# Impact of three-dimensional magnetic perturbations on turbulence in tokamak edge plasmas

B Luce, P Tamain, G Ciraolo, Ph Ghendrih, G Giorgiani, E Serre

▶ **To cite this version:**

HAL Id: hal-02939282

https://hal.science/hal-02939282

Preprint submitted on 15 Sep 2020

# Impact of three-dimensional magnetic perturbations on turbulence in tokamak edge plasmas

**B Luce[1,2], P Tamain[2], G. Ciraolo[2], Ph. Ghendrih[2], G. Giorgiani, and E Serre[1]**

[1] Aix-Marseille Univ., CNRS, Centrale Marseille, M2P2, Marseille, France
[2] CEA, IRFM, F-13108, St Paul-lèz-Durance, France

E-mail: eric.serre@univ-amu.fr

**Abstract.** The impact of resonant magnetic perturbations (RMP) on the plasma edge equilibrium and on the turbulence is investigated in a circular limited configuration. The study is based on a Braginski-based isothermal fluid model. The flow response of an unperturbated case to a small amplitude three-dimensional single mode RMP is studied and a scan in amplitude and poloidal and toroidal mode number is performed. Special attention is given when magnetic islands appear in the simulation domain on flux surfaces of rational safety factor. Results show an impact of Magnetic Perturbations (MPs) on both the plasma equilibrium and on the turbulence properties, with a deviation to the reference solution which depends on the MPs amplitude and on their wavenumbers. The impact of MPs on turbulence is however globally weaker than on the plasma equilibrium, suggesting a stabilizing effect of the MP on turbulent transport. Experimental trends are recovered such as the density pump-out and the increase of the radial electric field as well as the reorganization of the parallel velocity. The ballooning of the transport is modified under the effect of the perturbations, with a shift of the peaked poloidal region from the upper to the lower outer midplane. In the present model, the SOL width is observed decreasing in the presence of MPs. Turbulence properties are also impacted with the density fluctuations level decreasing in perturbated solutions and the intermittency is globally weakened.

## 1. Introduction

Heat and particle exhaust in future reactors like ITER remains one of the most critical issue for succeeding operation, due to the engineering limits of the materials taking the energy fluxes. This challenge became even more important with the discovery of the high confinement mode (H-mode) in ASDEX [1] (and subsequently most others diverted machines). While the improved confinement associated with H-mode makes it the regime of reference for the design and operation of ITER, it also comes with negative side-effects when looking at heat exhaust issues. In steady state, H-mode is associated with narrower Scrape-Off Layers (SOL) than in L-mode [2, 3], leading to predictions of the heat flux decay width in ITER of the order of 1mm and heat flux densities to the target larger than material limits. The strategy to cope with these conditions consists in running the machine in semi- or fully-detached conditions, i.e. in using energy loses generated in the divertor by neutral particles and impurities to dissipate radiatively the energy flux before it reaches the targets [4]. H-mode is also associated with MHD instabilities, the so-called Edge Localized Modes (ELMs), which generate transient heat and particle fluxes to the target plates [5]. Predictions for ITER are well beyond acceptable engineering limits [6], making it mandatory to implement a strategy to prevent the development of ELMs. Several methods have been proposed and will be implemented in ITER to mitigate ELMs, among which the most promising consists in the use of externally induced small resonant magnetic perturbations (RMPs, MPs). However, the introduction of these perturbations is not without consequence on the plasma equilibrium and could eventually impact the control of steady state fluxes by detachment.

MPs are by nature 3D and break the toroidal symmetry assumption made in the large majority of experimental and numerical studies. These MPs are called resonant when they resonate with the field on a given magnetic flux surface, usually located in the plasma edge region. The efficiency of these MPs at controlling ELMs depends on different conditions (see [7]) and the 3D full understanding of the complex interaction between RMP and the plasma remains a challenging task. Several experimental studies have underlined 3D changes on the heat flux and particle distribution at the egde plasma, for different tokamaks [8–10]. One of these effects is the non-axisymmetric pattern of the heat flux, which could have detrimental effect on the detachment. Among other known effects, we note the equilibrium modifications with a change of the radial electric field, of the plasma rotation and of the parallel flows [8]. Concerning turbulence, experiments show a change of the density fluctuations with a complex pattern remaining difficult to interpret [8].

On the simulations efforts, most studies concentrate on the plasma response to external MP, such as the plasma screening [11, 12] in a MHD framework or the coupling ELM-RMP [13] but little is known about the inter-ELM conditions. Up to now, most of

the focus has been given to evaluating the impact of RMPs on the access and toroidal symmetry of the detached regime. Such modelling requires a code combining 3D geometry and neutral physics. This is the case of EMC3-EIRENE [14] whose model relies on a mean-field approach, i.e. plasma transport equation in which perpendicular fluxes are assumed to take the form of a Fick's law with prescribed diffusion coefficients. In the absence of better information on the impact of RMPs on anomalous transport, these studies are conducted with fixed transport coefficients taken equal for both axisymetric reference cases and RMP-perturbed cases [15]. In this frame, 3D simulations show distinct differences in the pattern of the fluxes reaching the divertor compared to axisymmetric ones [16]. However, the assumption that perpendicular transport mechanisms are not significantly influenced by MPs needs to be checked as it might impact these results.

Understanding and evaluating the impact of MPs on perpendicular transport can only be made with the support of 3D edge turbulence codes. Moreover, the code must have a few specific features, including the capability to run with realistic magnetic geometry (at least a realistic safety factor profile) and a non-axisymmetric magnetic field. Very few tools actually match these requirements to date, explaining why efforts towards modelling the impact of MPs on edge turbulence have remained quite limited in the literature. Reiser *et al.* [17] modelled a full 3D circular geometry with both open (SOL) and closed (CFR) field lines using an electromagnetic fluid code. Their work showed a strong suppression of blob amplitude, and a reversal of the radial $E \times B$ flux when an ergodic MP is applied, in accordance with the experiments cited herein. This work was extended with [18] in a non-isothermal framework, showing a reduction of the pedestal profile gradients with the RMP, but little about turbulence itself.

With the lack of further studies with 3D fluid codes, the modelling effort of 3D edge plasma turbulence with 3D MPs is still needed. The main question of interest is the evaluation of the impact of the MPs on transverse transport in order to guide the modelling effort in mean-field tools. In particular, the amplitude and localization of such impact need to be quantified. Impact on fluctuations and global flows is also of interest as it might result in a change in impurities erosion and redistribution. In this paper, we investigate, with a fluid model, the impact of MPs on turbulent transport and equilibrium in the edge plasma of tokamaks. As first step before moving towards higher complexity, an isothermal model and a limiter configuration are used, and single mode perturbations are considered. The electrostatic TOKAM3X code, modified to introduce 3D magnetic perturbations, is used (see [19] for the version without MPs). Due to the electrostatic aspect of the model, the screening of the MP by the plasma [11, 12] and the magnetic flutter in the frame of plasma turbulence [18] are not taken into account in the present study. This is not a strong limitation as we work in ideal simplified conditions with low beta plasmas and single mode perturbations. The plasma screening will have to be taken into account when these studies are generalized to realistic RMP spectra and/or high beta discharges. In this sense, we assume being in the same framework as [20] and let any generalization to future work.

The rest of the paper is organized as follows. Sec. 2 briefly introduces the mathematical and numerical model as well as the implementation of a 3D MP in the TOKAM3X code. The impacts of MPs on the global edge plasma equilibrium and on the turbulence properties are investigated in Sec. 3, and in Sec. 4, respectively. Finally, a discussion on the $E \times B$ shear and the difference between turbulent and mean-field simulations are provided in Sec. 5 before the conclusion in Sec. 6.

## 2. Electrostatic fluid turbulence model with 3D magnetic perturbations

### 2.1. The TOKAM3X model

The TOKAM3X code is a two-fluid, drift-reduced electrostatic model for electrons and a single ion species, solving the edge (closed and open field line region) plasma in versatile geometries [21], based on the Braginskii's closure [22]. All details are provided in Ref. [19].

The code is run here in its isothermal version and in a circular limited geometry. A non-isothermal version of the code exists as seen in [23] and is able to run into complex and realistic geometries [21]. This allows us in this first work to exclude geometrical and non isothermal effects for a step-by-step approach. The dimensionless equations together with the boundary conditions for the particles density $N$, the parallel momentum $\Gamma$, the vorticity $W$ and the electric potential $\Phi$ are given in Appendix A. The reference scales for space and time are the ion Larmor radius $\rho_L = \sqrt{m_i T_0}/(eB_0)$, where $m_i$ is the ion mass and $e$ the elementary charge, and the inverse of the ion cyclotron frequency $\omega_c = eB_0/m_i$, respectively.

### 2.2. Magnetic equilibrium and perturbations

The equilibrium magnetic field $\vec{B}_0$ is assumed to be fixed and axisymmetric (toroidally symmetric) with the existence of flux surfaces, which are tangent to the magnetic field lines. The magnetic field orientation is such that the ion $\nabla B$ drift (Eq. A.6) is oriented toward the bottom of the machine. The safety factor $q$ is chosen with a parabolic profile, and varying between 3 and 6 within the simulation box. We consider here the addition of a three-dimensional perturbation with a small enough amplitude to remain in the model assumptions.

#### 2.2.1. Single mode MP case

The cylindrical basis is defined as $\vec{B} = \vec{B}(R, Z, \phi)$, where $R$ is the major radius, $Z$ the vertical distance and $\phi$ the toroidal curvilinear coordinate. As the magnetic field is divergence-free, it can be written as the curl of a vector potential $\vec{A}_0$:

$$\vec{B}_0 = \vec{\nabla} \times \vec{A}_0 \tag{1}$$

Due to the anisotropy of magnetically confined plasmas and the magnetic topology, it is natural to define a three-dimensional non-orthogonal local basis, a so-called curvilinear

system, such that each position vector $\vec{r}$ follows the transformation:

$$\vec{r}(R, Z, \phi) = \vec{r}(\psi, \theta^*, \varphi) \tag{2}$$

where $\psi$ labelled the flux surfaces, $\theta^*$ is a poloidal curvilinear angle, varying along flux surfaces (normalized between $[0, 2\pi]$) and $\varphi$ is a toroidal curvilinear angle (normalized between $[0, 2\pi]$). This allows to define a set of covariant $(\vec{e}_\psi, \vec{e}_{\theta^*}, \vec{e}_\varphi)$ and contravariant $(\vec{e}^\psi, \vec{e}^{\theta^*}, \vec{e}^\varphi)$ basis, such that:

$$\vec{e}_\psi = \frac{\partial \vec{r}}{\partial \psi} \; ; \; \vec{e}_{\theta^*} = \frac{\partial \vec{r}}{\partial \theta^*} \; ; \; \vec{e}_\varphi = \frac{\partial \vec{r}}{\partial \varphi} \tag{3}$$

$$\vec{e}^\psi = \vec{\nabla}\psi \; ; \; \vec{e}^{\theta^*} = \vec{\nabla}\theta^* \; ; \; \vec{e}^\phi = \vec{\nabla}\varphi \tag{4}$$

With these two basis, the magnetic vector potential, associated with the equilibrium field $\vec{B}_0$, can be written [24]:

$$\vec{A}_0 = \Psi_p \vec{\nabla}\varphi + \Psi_t \vec{\nabla}\theta^* \tag{5}$$

where $\Psi_p(\psi)$ and $\Psi_t(\psi, \theta^*)$ are flux fonctions (the indices stand for poloidal and toroidal respectively).

The small amplitude MP is introduced in TOKAM3X by disturbing the magnetic vector potential $\vec{A}_0$ as follows:

$$\vec{A} = \Psi_p(1 + \epsilon_p)\vec{\nabla}\varphi + \Psi_t \vec{\nabla}\theta^* \tag{6}$$

where $|\epsilon_p(\psi, \theta^*, \varphi)| \ll 1$ with

$$\epsilon_p = a \cdot 10^{-3} \sin(m\theta^* - n\varphi) \tag{7}$$

with $(m, n)$ are the wavenumbers in the poloidal and toroidal directions, respectively, and $a$ is the amplitude (not radially dependant). This perturbation being small, the computational grid can be kept axisymetric and aligned along the magnetic surfaces without introducing any numerical issues on the solution accuracy. This leads to the following relations for the components of the basis:

$$\vec{e}_\varphi \cdot \vec{e}_\psi = \vec{e}_\varphi \cdot \vec{e}_{\theta^*} = \vec{e}^\varphi \cdot \vec{e}^\psi = \vec{e}^\varphi \cdot \vec{e}^{\theta^*} = \vec{e}^\varphi \times \vec{e}_\varphi = 0 \tag{8}$$

and thus for the magnetic field to:

$$\vec{B} = \left(\frac{\partial \epsilon_p \Psi_p}{\partial \theta^*}\right)\vec{\nabla}\theta^* \times \vec{\nabla}\varphi + \left(\frac{\partial \Psi_p}{\partial \psi} + \frac{\partial \epsilon_p \Psi_p}{\partial \psi}\right)\vec{\nabla}\psi \times \vec{\nabla}\varphi + \left(\frac{\partial \Psi_t}{\partial \psi}\right)\vec{\nabla}\psi \times \vec{\nabla}\theta^*$$

$$= B^\psi \vec{e}_\psi + B^{\theta^*} \vec{e}_{\theta^*} + B^\varphi \vec{e}_\varphi = B_r \frac{\vec{e}_\psi}{|\vec{e}_\psi|} + B_p \frac{\vec{e}_{\theta^*}}{|\vec{e}_{\theta^*}|} + B_t \frac{\vec{e}_\varphi}{|\vec{e}_\varphi|} \tag{9}$$

where $B^i$ are the contravariant components of the magnetic field. $(B_r, B_p, B_t)$ are the radial, poloidal and toroidal components of the magnetic field. For an axisymmetric magnetic field, $B_r = 0$. With the new radial component $B_r$, the parallel and perpendicular operators and the drift velocities have to be recalculated and can be seen in Eq. A.1 A.2 A.3 A.4. Some details on the curvilinear form of the drifts are given in Appendix B.

## 2.3. Simulation settings

The simulations are run in circular geometry with an infinitely thin limiter located at the bottom of the machine. Open (SOL) and closed (CFR) fieldline regions are both simulated. To save computational time, only a half torus is modelled, assuming the $\pi$-periodicity of the solution in the toroidal direction.

*Geometrical parameters* - The aspect ratio is chosen $\mathcal{A} = \frac{a}{R_0} = 3.4$. The minor radius of the simulated tokamak is $256\rho_L$ (Larmor radius).

*Control parameters* - The normalized parallel resistivity $\eta_\parallel$ and the perpendicular diffusion coefficient $D_{\perp,X}$ are fixed in all simulations and equal to $\eta_\parallel(\frac{en_0}{B_0}) = 10^{-5}$ and $D_{\perp,X} = 10^{-2}(\rho_L^2 \omega_c)$. This value is of the order of the neoclassical values, and small enough to make sure turbulence is the dominant transport mechanism while preserving numerical stability.

Finally, a particle source is set at the inner boundary (core boundary). The source is radially decaying as a vanishing exponential after a few cells to ensure a constant particle source and to have no effect on the simulation away from the boundary.

| Simulation | $a$ | $m$ | $n$ |
|---|---|---|---|
| Reference | 0 | 0 | 0 |
| MP no island | 1 | 6 | 4 |
| | 2 | 6 | 4 |
| | 3 | 6 | 4 |
| | 1 | 10 | 6 |
| MP islands | 1 | 6 | 2 |
| | 1 | 15 | 4 |
| | 1 | 18 | 4 |
| | 1 | 22 | 6 |

**Table 1:** *Parameters $(a, m, n)$ of the MPs used in the simulations. $a$ is the amplitude, $m, n$ are the poloidal and toroidal wavenumbers, respectively. $n$ is given for a full torus.*

The mesh in $\psi \times \theta^* \times \varphi$ is $64 \times 512 \times 64$. Each simulation is run for longer time than the confinement time. The equilibrium is assumed to be reached when variations of the time derivatives for the density, the momentum and the particles flux at the limiter targets are less than 1%.

*Magnetic perturbations (MPs)* - The parameters of the perturbations Eq. 7 are given in Tab. 1. The case $(0, 0, 0)$ corresponds to the simulation of reference without MP. This reference solution has been used as an initial condition for all computations with MP. In agreement with the theory of MPs, depending on the wavenumbers of perturbated modes magnetic islands can be found in the simulation domain on flux surfaces of rational $q$. In this case, solutions are referred as solutions with magnetic islands. For some others modes, magnetic islands do not appear in the computational domain (their amplitude are actually too weak to break the flux surfaces). These solutions are referred as solutions without magnetic island. An illustration of such solutions is given on Fig. 1. It shows two Poincaré sections corresponding to magnetic perturbations $(a, m, n) = (1, 6, 4)$ (Fig. 1a) and $(a, m, n) = (1, 6, 2)$ (Fig. 1b). On Fig. 1b, multiple magnetic islands chains can be seen at different radial locations on the flux surfaces of rational $q = m/n$ as $3 \leq q = 6/2 \leq 6$. This is explained by the form of the poloidal magnetic field which writes as $B_p \propto 1/[R_0(1 + \mathcal{A}\cos\theta^*)]$. Expanded in a Taylor series, the multiplication of $B_p$ by the perturbation $\epsilon_p$ (Eq. 7) involves successive modes and not only the mode excited by the perturbation of $\Psi_p$. On the example of

Fig. 1b multiple modes can appear as long as $3 \leq q = i/2 \leq 6$, that corresponds to $i = 6, 7, \ldots, 12$. The amplitude of the magnetic islands however decreases when the mode $m$ increases.



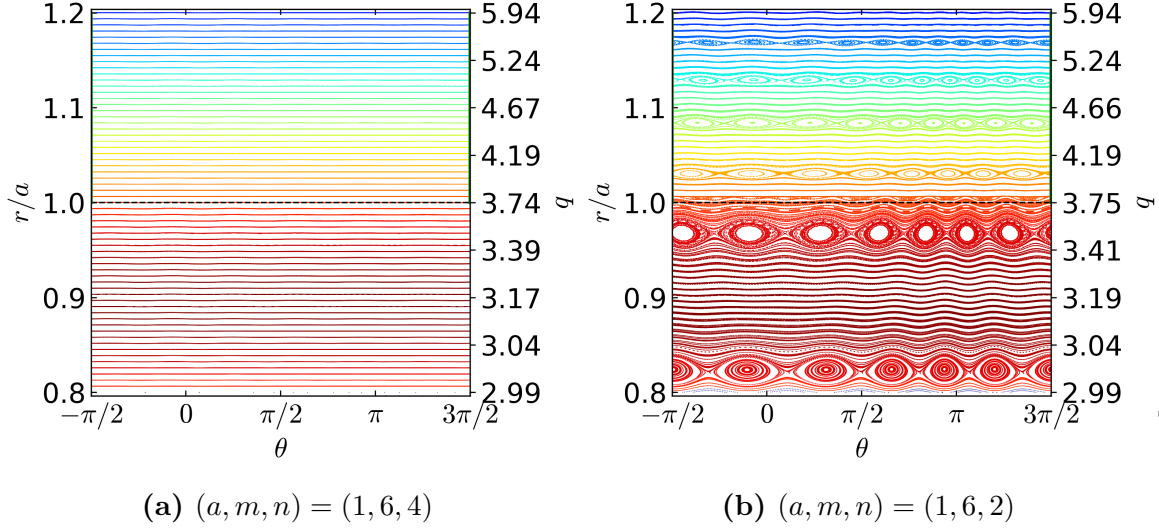**(a)** $(a, m, n) = (1, 6, 4)$          **(b)** $(a, m, n) = (1, 6, 2)$

**Figure 1:** *Poincaré sections of the perturbed magnetic field for two MPs. The values of the safety factor q have been plotted on the vertical axis on the right hand. (1a) No magnetic islandin the computational domain. (1b) Magnetic islands at q = 6/2, 7/2, 8/2, ... $\theta^* = 0$ corresponds to the Low Field Side (LFS) mi plane location. Increasing $\theta^*$ direction corresponds to the electron diamagnetic direction.*

In the poloidal and toroidal directions, the response of the magnetic field to any MP is as expected. It is shown in the poloidal direction on Fig. 2. The Fourier transforms of the norm of the total magnetic field $|\vec{B}|$ show that peak values correspond to the poloidal $m$ mode of the perturbation, with a secondary peak of smaller amplitude corresponding to a resonance at $2m$. The peaks become more visible for high $m$, typically $m \geq 10$, specially when magnetic islands appear in the simulation box, Fig. 2b. Results in the toroidal direction are not shown, the spectra being simply composed of two peaks, one at $n = 0$ corresponding to the toroidal component of the magnetic field and the other one to the wavenumber of the perturbation.

## 3. Impact of three-dimensional single MP on the mean fields

The impact of MPs is analyzed on flow variables averaged on time and in the toroidal direction.

### 3.1. Density pump-out

The first observation is the density pump-out for most MP. This can be seen on the time trace of the particle content on Figs. 3. We can clearly see that as soon as the MP is
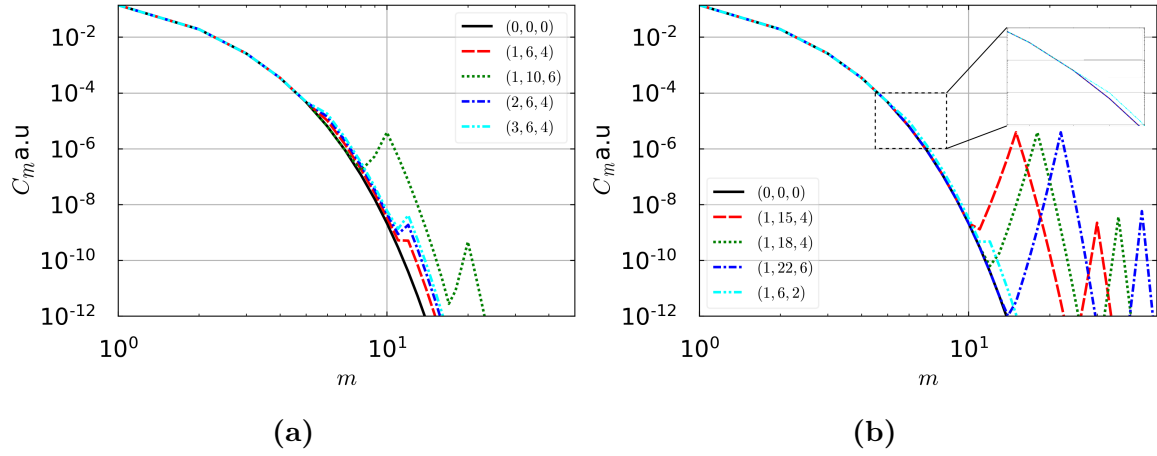
**(a)**

**(b)**

**Figure 2:** *Fourier transforms in the poloidal direction of the norm of the total magnetic field $|\vec{B}|$ for different MPs without (2a) or with (2b) magnetic islands inside the computational domain. $r/a = 0.9$ and $\varphi = \pi/8$. $C_m$ is the energy for each mode $m$.*

activated, the particle content drop by a few percent (5 to 10% at most), which is a clear reminiscent of the the density pump-out seen in experiments in DIII-D [25], JET [26] or MAST [8]. We observe a pump-out for all perturbated cases for the simulations without magnetic island (see Fig. 3a) with a greater amplitude for the cases $(2, 6, 4)$ and $(1, 10, 6)$. It seems that a threshold exists as the case $(3, 6, 4)$ is similar to $(1, 6, 4)$ in respect to the amplitude of the pump-out. For the cases with magnetic islands (see Fig. 3b), the maximal pump-out is for the cases $(1, 15, 4)$ and $(1, 6, 2)$ whereas the case $(1, 22, 6)$ could almost be seen as a pump-in. No visible trends seems to be highlighed concerning the pump-out effect in respect to the mode numbers or the amplitude of the perturbation.
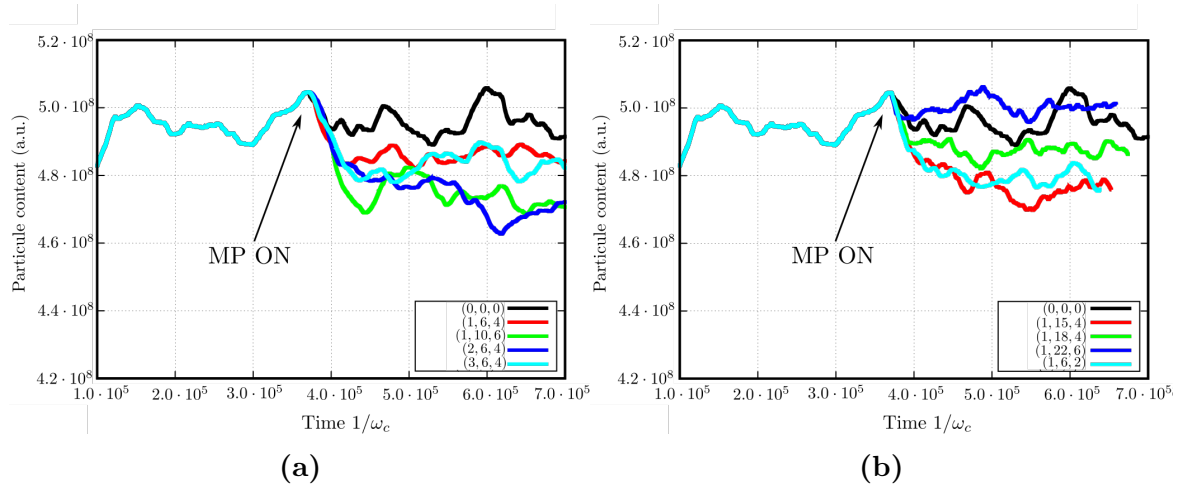


**(a)**

**(b)**

**Figure 3:** *Time traces of the particle content in the simulation box for the case with magnetic islands outside the box (3a) and inside (3b).*

## 3.2. Mean profiles

Present results show that the impact of the MPs is the strongest on the LFS. The plots on Fig. 4 show the radial density profiles in log scale at the Low Field Side (LFS) midplane. In the far closed field lines region (CFR), it shows that whatever the MP the radial gradient remains unchanged while the density is reduced. Then, just before the separatrix, the gradient decreases compare to the reference. It peaks at the separatrix, with a lower peak for most MPs. The density profiles show a higher density when MP are on. The gradient decreases after the separatrix, in the same way, with or without MPs. Deeper into the SOL, the density profiles flatten, having a mostly higher gradient. For the MPs without magnetic island in the simulation box (Fig. 4a), the density deviation from the reference solution increases with the MP amplitude (see solutions $(1, 6, 4)$, $(2, 6, 4)$) but seems to have a threshold as solutions $(3, 6, 4)$ and $(2, 6, 4)$ are really similar. The solution $(1, 10, 6)$ behaves almost similarly than the solution $(2, 6, 2)$, whose changes are starker than the similar amplitude $(1, 6, 4)$. Thus, even without magnetic island, the response of the density profile can be impacted in similar way with either a higher amplitude with lower mode number or a lower amplitude but with higher mode number of the perturbation.

For the MPs with magnetic islands in the simulation box (Fig. 4b), the density changes similarly and the density deviation from the reference solution changes with the MP wavenumber, the amplitude, here, being the same for all MPs. The changes are however more pronounced than in the solutions without magnetic island. Density gradients decrease more sharply around the separatrix under the effect of the resonant MPs (see Figs. 4c and 4d). It results in a higher density around the separatrix for these MPs.

The density profile is the first visible change in experiments with MPs. A second one is the profile of the radial electric field, directly impacted by the new radial component of the magnetic field. Figs. 5 show the radial profiles of the mean electrostatic potential $\Phi$ at the LFS midplane. The impact of MPs depends on the presence of magnetic islands or not in the simulation box. Without magnetic islands (Fig. 5a), an increase is observed for most studied cases in the CFR as well as a global drop in the SOL, leading to a flattening of the profile. The direct consequence is a decrease (in absolute value) of the radial electric field $E_r$. This trend is observed experimentally too [8, 27, 28]. With magnetic islands (Fig. 5b), the shift of potential is a global increase in both CFR and SOL, except in the far SOL where the potential decreases below the reference value of the non perturbated solution. We observe that the amplitude of the increase for the electric potential is dependent on both the mode and the amplitude. Higher modes $(m, n)$ or higher amplitudes $a$ seem to increase the rise of the electric potential.

Figs. 5c,5d show the radial profiles of the mean radial electric field at the LFS midplane. As a side note, the HFS midplane profile follows the same trend. For the cases without magnetic island in the simulation box (Fig. 5c), the flattening of $E_r$ on perturbated solutions, hints by the profile of $\Phi$, is confirmed. The mean radial electric field, negative in the CFR in the reference simulation, shifts towards positive values

**(a)** *No magnetic island*

**(b)** *Magnetic islands*



**(c)** *No magnetic island*
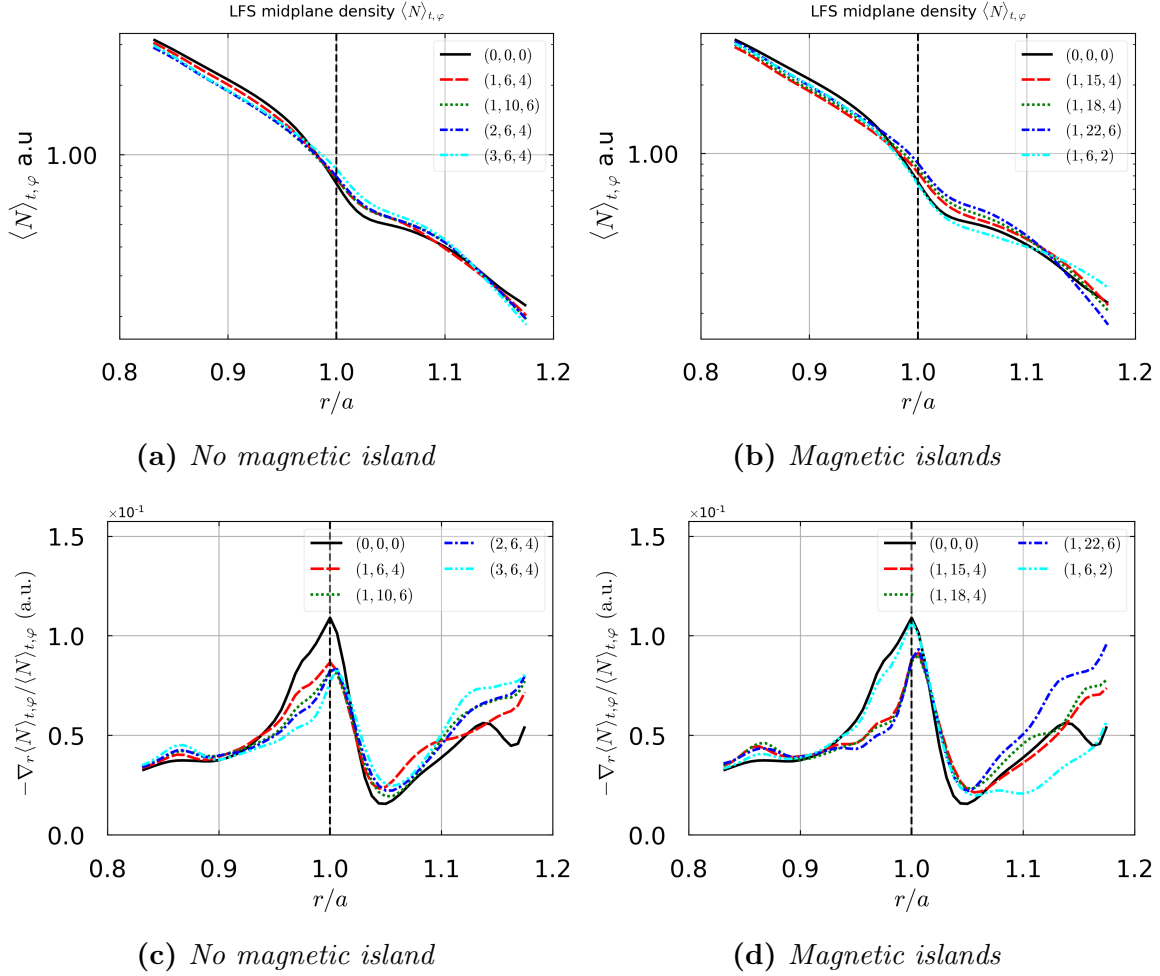
**(d)** *Magnetic islands*

**Figure 4:** *Radial profiles of the mean density (4a,4b) in log scale and of the density radial gradient (4c,4d) at the LFS midplane for different magnetic perturbations (MPs). MPs with no magnetic island in the simulation box (4a,4c). MPs with magnetic islands (4b,4d). Quantities are averaged on time t and toroidal direction $\varphi$. The vertical dashed line is the separatrix.*

resulting in a much lower amplitude. Deeper into the SOL, the mean radial electric field flattens with respect to the reference solution but the profiles become nearly independent on the MP.

For the cases with magnetic islands (Fig. 5d), in the CFR, the mean radial electric field shifts in the same manner with the MP wavenumber. In the SOL near the separatrix, $E_r$ sharply increases, with an increasing radial gradient with the MPs amplitude, then decreases to a plateau in the far SOL.

This flattening of the electric potential and the resulting drop of the radial electric field can have direct consequences on the parallel flows, and this is the object of the following section.
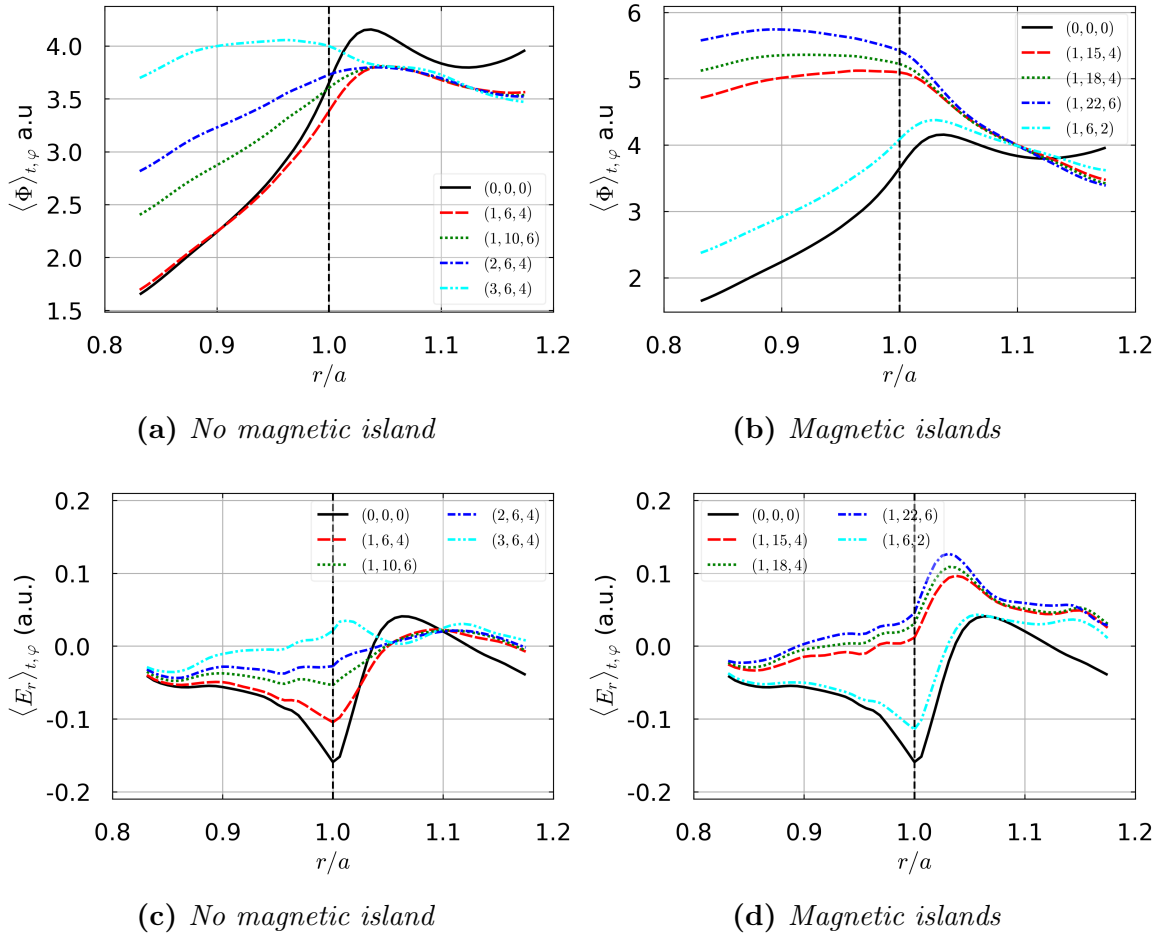
**(a)** *No magnetic island*

**(b)** *Magnetic islands*



**(c)** *No magnetic island*

**(d)** *Magnetic islands*

**Figure 5:** *Radial profiles of the mean electrostatic potential $\Phi$ (5a,5b) and of the mean radial electric field $E^r = \langle -\partial_r \Phi \rangle_{t,\varphi}$ (5c,5d) at the LFS midplane for different magnetic perturbations (MPs). MPs with no magnetic islands (5a,5c) in the simulation box. MPs with magnetic islands (5b,5d). Quantities are averaged on time t and toroidal direction $\varphi$. The vertical dashed line is the separatrix.*

### 3.3. Impact on flows and rotation

The increase of the potential, and consequently the change in the radial electric field, leads to a reorganization of the plasma rotation and flows which is illustrated by a change of the parallel velocity. Parallel velocities have been experimentally measured in [8] and can be a point of qualitative comparison with the simulations. Fig. 6 shows the radial profiles of the mean parallel Mach number ($M_\parallel = \Gamma/(N\sqrt{2})$) averaged on time and on the toroidal direction at the LFS (Figs. 6c and 6d) and HFS (Figs. 6a and 6b) midplanes. A positive Mach number corresponds to the electron diamagnetic direction.

At the HFS midplane, in the cases with MPs without island in the simulation box, Fig. 6a shows a decrease of $M_\parallel$ in the perturbed solutions around the separatrix with a complete reversal of the sign of $M_\parallel$. In the far SOL and in the far CFR, the variations with respect to the reference case are very small. In the cases with magnetic islands in

the simulation box, Fig. 6b shows similar trends around the separatrix but a significant increase of $M_\parallel$ in the far SOL and a more significant increase in the far CFR than in the cases without magnetic islands. We note that the decrease (or increase if relevant) is more pronounced for high amplitudes or high mode numbers.

At the LFS midplane (Figs 6c and 6d), all cases show similar trends with a global increase of $M_\parallel$ in perturbated solutions, with still a stronger increase for higher modes or amplitudes. On Fig. 6d, the presence of magnetic islands leads to a larger rise of the profiles. As the reference value of $M_\parallel$ is negative at the LFS midplane, the progressive increase depending on the MP has different meaning. For low amplitude and modes MPs, such as $(1, 6, 2)$ and $(1, 6, 4)$, the increase of $M_\parallel$ is actually a decrease of the parallel flow as it tends to zero. For larger amplitudes or modes, the MPs create a positive parallel flow, so that the increase is both a change in the direction of the flow and an increase of the speed of the flow. This trend is observed in [8], at least in the SOL. In the CFR, the parallel flow is shown to increase, which we only observed at the HFS midplane.

### 3.4. Impact on radial transport

In order to better understand the changes in the radial profiles of the density $N$ and the potential $\Phi$ on the global plasma behavior, the different components of the radial flux are analyzed. As the simulation is flux-driven, and the forcing value of the flux is constant through all simulations, the radial particle flux is constant. The radial particle flux can be decomposed into 5 components:

$$\Gamma^r = \Gamma^r_{E \times B} + \Gamma^r_{\nabla B_i} + \Gamma^r_{\text{curv}} + \Gamma^r_{\text{diff}} + \Gamma^r_\parallel \tag{10}$$

The terms successively denote the $E \times B$ velocity driven flux (comprising a mean-field and a turbulent component), responsible of the turbulent transport, two contributions of the 2 curvature driven drifts i.e. the $\nabla B_i$ flux and the curvature one, the diffusive flux and the last one the radial component of parallel flux. The latter is non zero only when MP are turned on.

### 3.4.1. Flux surface averaged fluxes

The mean flux is estimated here by integrating each component along the flux surface (in $\theta, \varphi$), then average in time. The $E \times B$, the $\nabla B_i$ and the curvature components are shown on Fig. 7 at LFS. The diffusive component is shown on Fig. 8. The radial component of the parallel flux is neglectable even with MP and will thus not be discussed here. To give an order of magnitude, the contribution of $\Gamma^r_\parallel$ flux is $< 1\%$ of the total flux in all cases.

In the CFR, both the $E \times B$ and $\nabla B_i$ fluxes slightly increase near the separatrix, that is compensated by an equivalent decrease of the diffusive flux due to the response of the gradient, in both cases with or without magnetic islands. The changes are more complex in the middle and far SOL. For the cases without magnetic island, the $E \times B$ flux (Fig. 7a) decreases in the far SOL, which is partially compensated by an increase of the diffusive flux (Fig. 8a). For the cases with magnetic islands, the trend is a growth
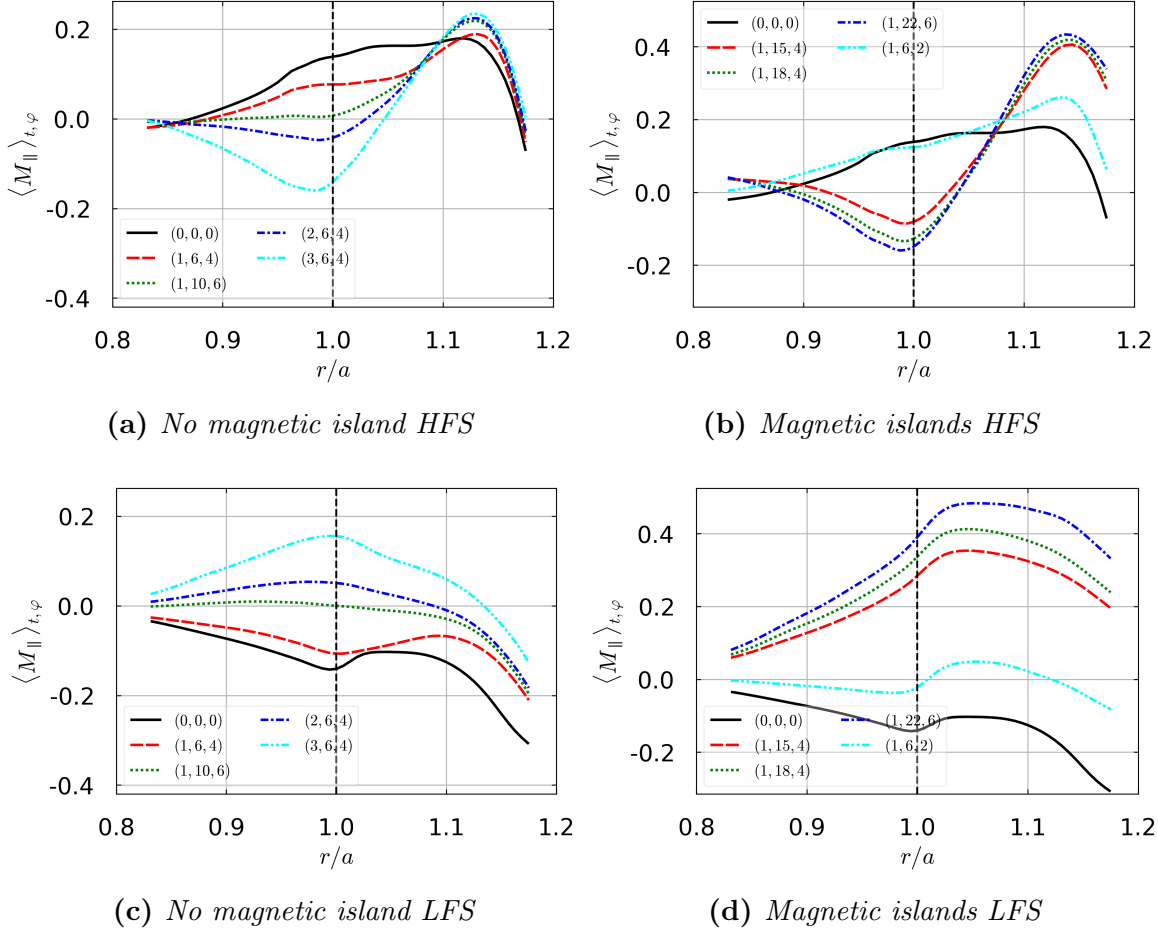
**(a)** *No magnetic island HFS*

**(b)** *Magnetic islands HFS*

**(c)** *No magnetic island LFS*

**(d)** *Magnetic islands LFS*

**Figure 6:** *Radial profiles of the mean parallel Mach number $M_\parallel = \Gamma/(N\sqrt{2})$ averaged on time and in the toroidal direction at the LFS (6a,6b) and at the HFS (6c,6d). MPs without magnetic island in the simulation box (6a,6c) and with magnetic islands (6b,6d). The vertical dashed line is the separatrix.*

of the $E \times B$ flux in the middle SOL (Fig. 7b) but a decrease in the far SOL. The diffusive flux increases comparably to the decrease of the $E \times B$ flux (Fig. 8b). As a note, the $\nabla B_i$ flux is negative (Figs. 7c and 7d), that explains why the sum of the $E \times B$ and the diffusive fluxes is above 100%. Finally the curvature drift shows an interesting behavior as the case without magnetic island (Fig. 7e) is not impacted whereas the case with magnetic island (Fig. 7f) shows a decrease in the SOL dependent on the mode number. These observation demonstrate a direct impact of the MPs on radial transport mechanisms, explaining the changes in density profiles and the density pump-out. A more detailed analysis of the impact on turbulence properties is proposed in Sec. 4.

*3.4.2. Poloidal distribution of $\langle \Gamma^r \rangle_{t,\varphi}$.* In order to explain the changes in the parallel flow velocity, we now investigate the poloidal distribution of radial fluxes. Indeed, the time average parallel flow in the edge plasma is driven by 2 mechanisms: the sheath loss
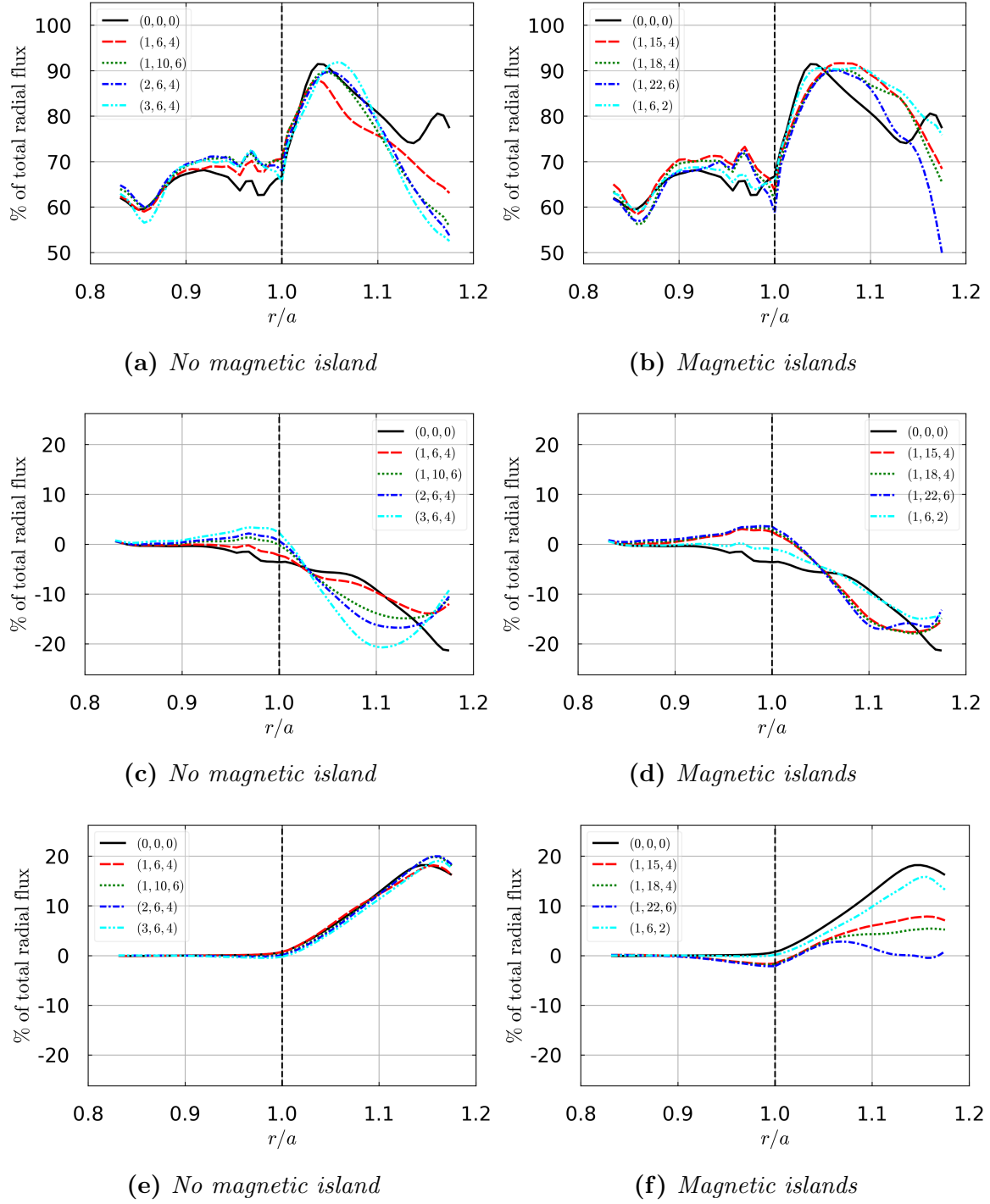
**(a)** *No magnetic island*

**(b)** *Magnetic islands*

**(c)** *No magnetic island*

**(d)** *Magnetic islands*

**(e)** *No magnetic island*

**(f)** *Magnetic islands*

**Figure 7:** *Radial profiles of the mean $E \times B$ flux $\Gamma^r_{E \times B}$ (7a, 7b), $\nabla B_i$ flux (7c, 7d) and curvusive flux $\Gamma^r_{\mathrm{curv}}$ (7e, 7f) at LFS. Cases without magnetic island (7a, 7c, 7e) in the simulation box. Cases with magnetic islands (7b, 7d, 7f) in the simulation box. The quantities are averaged both in time t and in the poloidal and toroidal directions $(\theta, \varphi)$. The vertical dashed line denotes the separatrix*

**(a)** *No magnetic island*  **(b)** *Magnetic islands*
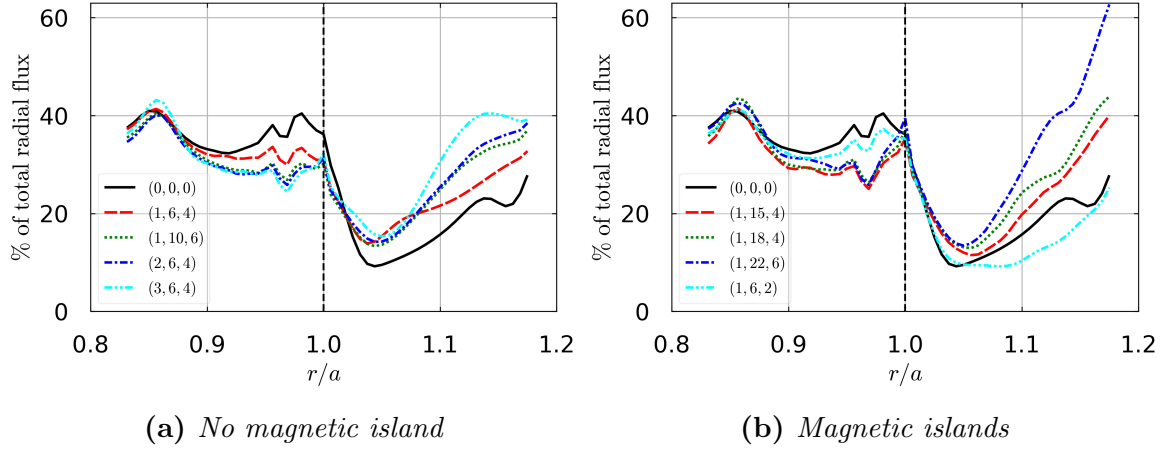
**Figure 8:** *Radial profiles of the mean diffusive flux $\Gamma_{\text{diff}}^r$ (8a,8b) at LFS. Cases without magnetic island (8a) in the simulation box. Cases with magnetic islands (8b) in the simulation box. The quantities are averaged both in time t and in the poloidal and toroidal directions $(\theta, \varphi)$. The vertical dashed line denotes the separatrix.*

at boundary conditions and the necessity to balance the local divergence of the radial flux ($\vec{\nabla} \cdot \vec{\Gamma} = 0$). The poloidal distribution and the asymeties of radial fluxes hence are crucial in the understanding of the changes on parallel flows $M_{\parallel}$. For each quantity we note:

$$f(t, \psi, \theta^*, \varphi) = \bar{f}(\psi, \theta^*, \varphi) + \tilde{f}(t, \psi, \theta^*, \varphi) \tag{11}$$

where $\bar{f} = \langle f \rangle_t$ is averaged over time and $\langle \tilde{f} \rangle_t = 0$ per construction. We are interested here at the time averaged fluctuating parts, so that only the product of two (or more) fluctuating parts remains.

We concentrate our study on the flux and more specifically here on $\Gamma_{E \times B}^r$ which in isothermal simulations is the only one component getting a non zero fluctuating part when averaged on time, $\propto \langle \tilde{N} \vec{B} \times \vec{\nabla} \tilde{\Phi} \rangle_t$. Fig. 9 shows the poloidal mean profiles related to $\Gamma_{E \times B}^r$ and averaged in time and in the toroidal direction at the flux surface $r/a = 0.9$. The Fig. 9a clearly shows a shift to the LFS midplane ($\theta = 0$) of the ballooning of the total $\Gamma_{E \times B}^r$ mean flux when the solution is perturbated by MP. This shift is larger when magnetic islands are in the simulation box as shown on Fig. 9b. This change in the poloidal asymmetry is directly related to the change of $M_{\parallel}$. This is underlined by the complex role plays by the mean and fluctuating parts of the flux.

If the fluctuating part is the major contribution of the flux (see on Figs. 9e and 9f) with an increase of the ballooning in the upper LFS midplane, the mean-field part varies the most. The mean contribution shows a complete reversal (see on Figs. 9c and 9d) around the LFS midplane.

The others mean-field contributions, $\Gamma_{\nabla B_i}^r$ and $\Gamma_{\text{curv}}^r$, are not shown here as their variations are at least one order of magnitude lower than the $E \times B$ mean-field variations. Furthermore, the most varying part, the $\Gamma_{\text{curv}}^r$ for the case with magnetic island, shows

a similar profile as the mean-field $E \times B$ with an increase at the bottom of the machine and a decrease at the top, the reference case being completely flat.

The main conclusion of this part is that the MPs create a poloidal redistribution of the radial fluxes, especially the mean-field part and particularly the $E \times B$ flux. This is linked to the poloidal reorganization of the density and it is in agreement with the parallel flow changes.

## 3.5. SOL width

The flux reorganization drives toward a study of the impact of the MPs on the SOL width. The decrease of the density in the SOL can be approximated into an exponential decay such that $\partial_\psi \langle N \rangle_t = \langle N \rangle_t / \lambda_N$ where $\lambda_N$ is the density gradient length, sometimes called the density decay length. The impact of MP on $\lambda_N$ is shown in Tab. 2. The values are obtained through an exponential fit of the density in the SOL. Except for the perturbation $(1, 6, 2)$ with an increase of around 10%, the density decay length decreases when the solution is perturbated. This decrease is of the order of 20%, and curiously of similar order for every MP. The mechanism of the drop of $\lambda_N$ can be seen as a consequence of the flow reorganization discussed before.

| Density decay length (in $\rho_L$) | | |
|---|---|---|
| MP | $\langle \lambda_N \rangle$ | Trend |
| $(0, 0, 0)$ | 36 | — |
| MP no island | | |
| $(1, 6, 4)$ | 30 | ↘ |
| $(2, 6, 4)$ | 30 | ↘ |
| $(3, 6, 4)$ | 28 | ↘ |
| $(1, 10, 6)$ | 30 | ↘ |
| MP islands | | |
| $(1, 6, 2)$ | 41 | ↗ |
| $(1, 15, 4)$ | 33 | ↘ |
| $(1, 18, 4)$ | 31 | ↘ |
| $(1, 22, 6)$ | 29 | ↘ |

**Table 2:** *SOL density decay length $\lambda_N$ (in Larmor radius $\rho_L$) averaged in poloidal and toroidal direction*

This is what has been seen in Fig. 4 except for the perturbation $(1, 6, 2)$. The solutions also show a steepening of the radial density gradient, which is also a reason for the decrease in $\lambda_N$. The particularity of $(1, 6, 2)$ can not be explained but we underline, that it is an extremum in the scan in mode numbers with larger islands than the others.

## 4. Impact of MP on turbulence properties

We have seen in the previous section that MPs impact the plasma equilibrium via a reorganization of particles fluxes, including the radial flux driven by turbulence. Changes in the properties of fluctuations has also been reported experimentally as a signature of the impact of MP on the edge plasma [8, 29]. Here, the impact of the MPs on turbulent fluctuations is analyzed.

Quantities are decomposed into a mean and a fluctuating part as presented in Eq 11. The fluctuations properties are analyzed from Probability Density Functions (PDFs).
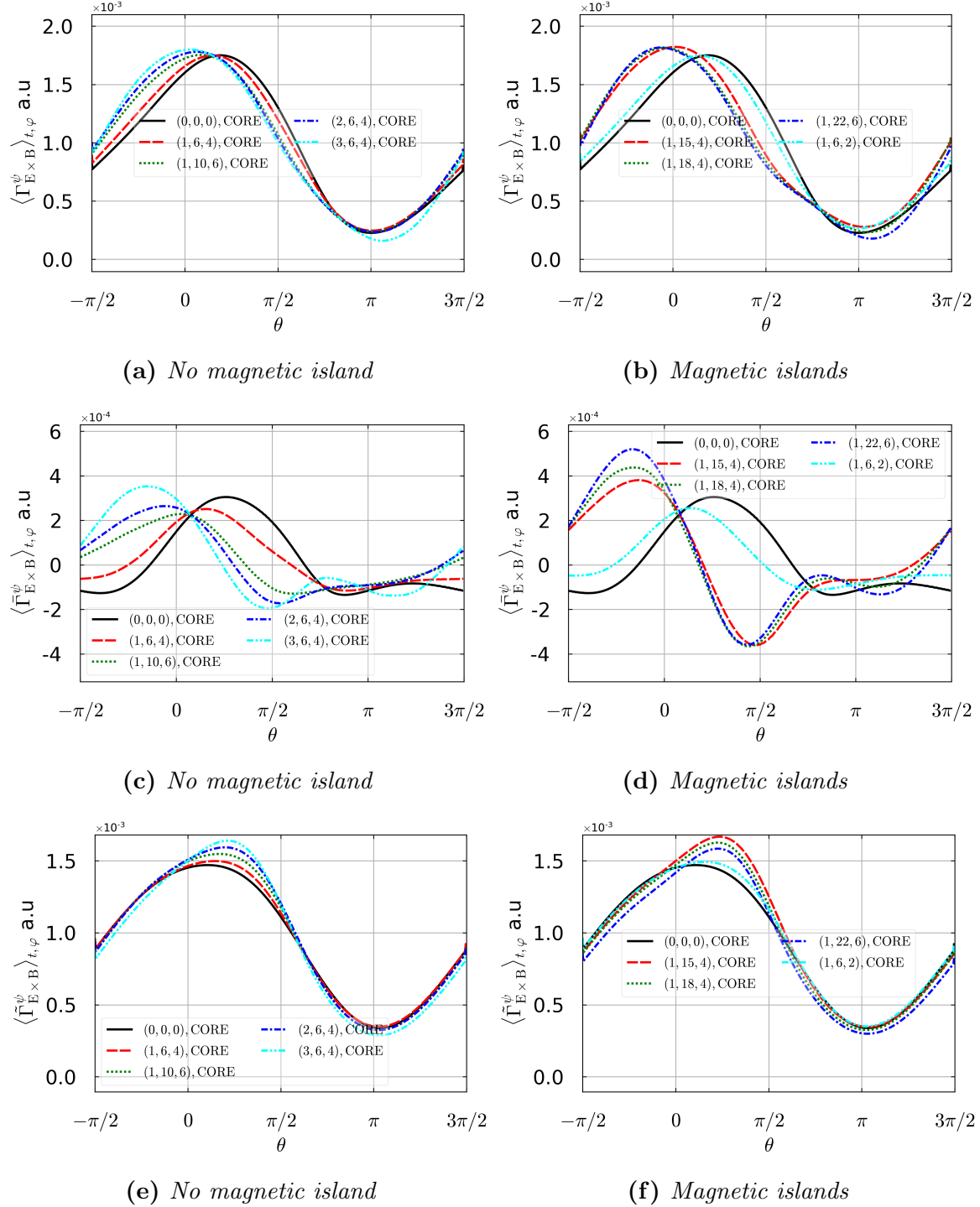
**(a)** *No magnetic island*

**(b)** *Magnetic islands*

**(c)** *No magnetic island*

**(d)** *Magnetic islands*

**(e)** *No magnetic island*

**(f)** *Magnetic islands*

**Figure 9:** *Poloidal profiles of the $E \times B$ total flux $\Gamma^r_{E \times B}$ (9a,9b), the mean $\bar{\Gamma}^r_{E \times B}$ (9c,9d) and the fluctuating $\tilde{\Gamma}^r_{E \times B}$ (9e,9f) parts at $r/a = 0.9$ (CFR). Quantities are $(t, \varphi)$-averaged. (9a,9c,9e) cases without magnetic island in the simulation box. (9b,9d,9f) cases with magnetic islands in the simulation box. $\theta = 0$ corresponds to the LFS midplane.*

The skewness for any variable $X$ is defined here as:

$$\gamma_1(X) = E\left[\left(\frac{X - \mu_X}{\sigma_X}\right)^3\right] \tag{12}$$

where $\mu_X$ is the mean and $\sigma_X$ the standard deviation of $X$.

### 4.1. Impact on the fluctuation levels

The evolution of the fluctuation level for density events in the radial direction, characterized here by the toroidal averaged of $\sigma_N/N$, is shown on Fig. 10. To compare both the difference with or without magnetic island and the poloidal asymmetry of the turbulence, the standard deviation is plotted at the HFS and the LFS midplane.

At the HFS midplane on Figs. 10a and 10b the fluctuation level in the CFR is low (of the order of 5%) and rather constant in the radial direction up to the vicinity of the separatrix. This trend remains unsensitive to MPs, whether magnetic islands are present or not. On the contrary, MPs have a clear impact on the density fluctuation level in the SOL. In this region, MPs reduce the fluctuation level from around 25% down to 15 to 20% depending on cases. In the cases with no magnetic island, the lowering of fluctuation level is nearly independent of the MP, whereas it becomes very sensitive to the perturbations wavenumber in the cases with magnetic islands. In these cases, the difference in the fluctuations level with the unperturbated case increases with $r/a$ and with the poloidal wavenumber $m$ of the perturbations.

At the LFS midplane on Figs. 10c and 10d, the fluctuations level in the CFR rapidly and continuously increases with $r$ independently of the MP, from 10% at the core boundary to 25% at the separatrix. The difference of amplitude with the HFS illustrates the ballooned character of turbulent transport already mentionned in Sec. 3. In the SOL and in the vicinity of the separatrix, the fluctuation level decreases with respect to the unperturbated case. The differences are larger in the cases with magnetic islands from barely 1% without islands and now up to 5%. Deeper into the SOL, perturbated solutions exhibit oscillating fluctuations around the reference case. Without magnetic islands, the fluctuation level follows the reference case minus 1% at most before going up to at most 8% after the mid SOL. With magnetic islands, the fluctuation levels start aroud minus 5% at the lowest point before going up by 5% at most after the mid SOL. No regular trend depending on amplitudes or modes of the MP is visible. Such a drop in the density fluctuations around the separatrix is in agreement with the decrease of the SOL width $\lambda_N$ and the increase of the density gradient in a large part of the SOL as seen in Sec. 3.

### 4.2. Impact on the turbulence intermittency

The PDFs of the density are plotted on Fig. 11 at two radial locations in the CFR and into the SOL at LFS midplane, i.e. $r/a = 0.975$ and $r/a = 1.0188$, respectively. Both locations correspond to a region with magnetic islands (if relevant). The color
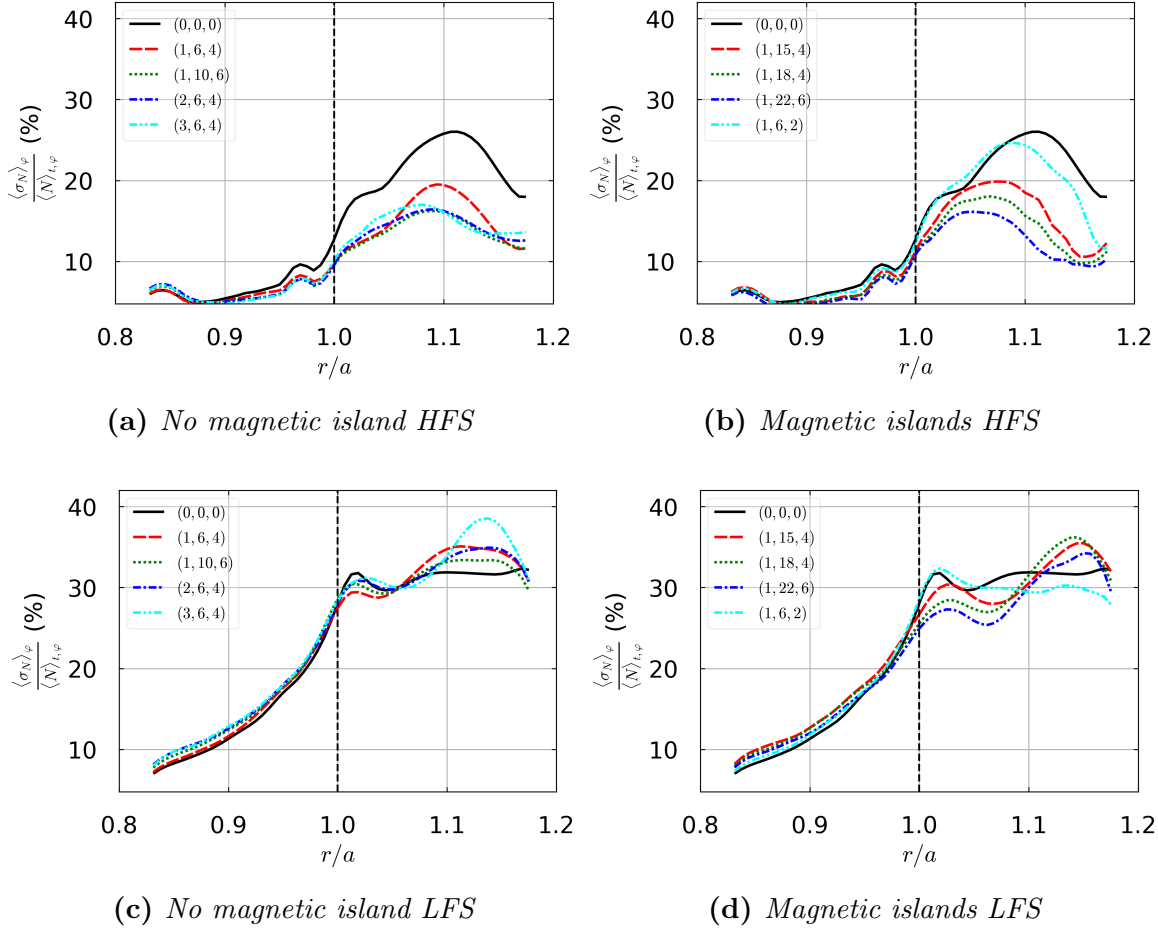
**(a)** *No magnetic island HFS*

**(b)** *Magnetic islands HFS*

**(c)** *No magnetic island LFS*

**(d)** *Magnetic islands LFS*

**Figure 10:** *Radial profiles of the standard deviation over time of the density averaged in the toroidal direction $\varphi$ and normalized by the $(t, \varphi)$-averaged density at the HFS (10a,10b) and at the LFS (10c,10d). Cases with no magnetic island 10a,10c in the simulation box. Cases with magnetic islands 10b,10d. The values are multiplied by 100 for readability. The dashed line is the separatrix.*

zones correspond to the direct histogramm of the event and the curves are obtained through a kernel density estimation. In the outer part of the CFR, the PDFs of the perturbated solutions are nearly Gaussian for the case without magnetic island (see Fig. 11a). The cases with magnetic islands (see Fig. 11b) show a positive skewness (skewed to the right), which seems stronger for higher mode numbers. Deeper inside the CFR (not shown here), the PDFs are not significantly perturbed by the MP and exhibit a gaussian shape.

In the SOL, the PDF of the reference case shows a PDF shape characterized by intermittent turbulence with a well-marked positive skewness with most event concentrated on the left of the figure (see Figs. 11c and 11d).

For the case without magnetic island (Fig. 11c), the PDF skews to the right, similarly with the reference case, which is still a mark of intermittency. Nevertheless,

with higher amplitude (or mode number), the peak of the curve decreases, forcing the distribution toward a less skewed profile. It could mean a loss of intermittency or, at least, a loss a high density bursty events compare to the average ones.

For the case with magnetic islands (Fig. 11d), the peaks of the PDFs decrease immediately for all MPs with no visible trends. The PDFs are still skewed to the right but as for the cases without magnetic island, the PDFs tends toward a gaussian shape, compare to the reference case. This is promising as we could expected a control of the turbulence properties in the SOL by the size and/or the numbers of magnetic islands, beyond the ELM suppression in H-mode.

These results show that the MPs do not change the turbulence properties in the CFR. The changes occur mainly near the separatrix and in the SOL with an opposite effect between the HFS and LFS midplanes. At the HFS midplane, the intermittency and bursty behavior of the turbulence increases while the effect is opposite at the LFS midplane. The intermittency still exists but with less high density (bursty) events.

The radial profiles of the skewness of the density along the time axis are now shown on Fig. 12 at both HFS and LFS. It is noted $\gamma_{1,N}$ and it is averaged in the toroidal direction. For each plot, the error barr is estimated lower than 5%. In the CFR, all plots show that the impact of MPs is weak, with a nearly zero skewness in this region. This means that as in the reference solution density events stay clearly well centered around the mean value with no favorable events (bursts or sinks). These plots show, for all cases, a larger skewness on the LFS midplane than on the HFS corresponding to the turbulence ballooning already mentionned.

In the SOL, the impact of perturbations is stronger than at the CFR. At the HFS midplane and with respect to the reference solution (Figs. 12a and 12b), there is a small decrease of the skewness near the separatrix, this effect being more pronounced in the case without magnetic island, followed by a large increase in the middle of the SOL, this effect is larger in the case with magnetic islands. For non resonant modes (Fig. 12a), there is no clear dependence of the solution on the wavenumber or the amplitude of the pertubation even if the perturbation of largest amplitude has the largest skewness all the others behave fairly similarly. For resonant modes (Fig. 12b), MP of high wavenumbers lead to a high positive skewness. As a final overall trend at HFS midplane, we can see that MPs seem to shift spacially to the left the behavior into the SOL of the density events (the events arising earlier with MP).

At LFS midplane, without or with magnetic islands, the largest changes concentrate into the SOL. For non resonant modes and with respect to the reference solution, the skewnesses of the perturbed solutions are smaller in the vicinity of the separatrix and then become larger deeper into the SOL, Fig. 12c. These deviations become larger when the amplitude of the perturbation is increased. We note an increase of the skewness in the far SOL. A similar trend is observed with magnetic islands, but the skewness remains smaller than the reference solution even in the far SOL (see Fig. 12d). The deviation becomes larger with the mode wavenumber.
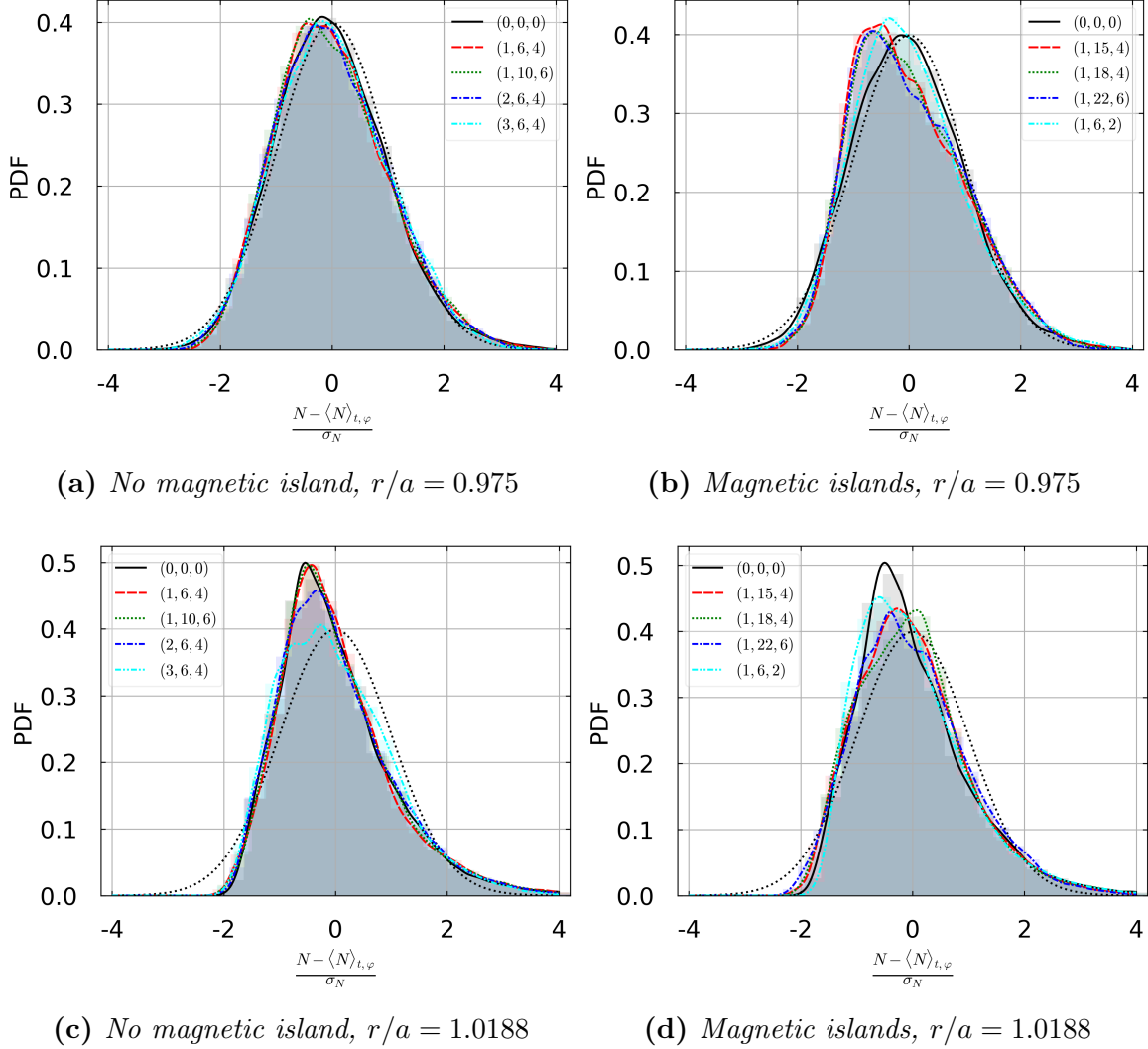
**(a)** *No magnetic island, $r/a = 0.975$*

**(b)** *Magnetic islands, $r/a = 0.975$*

**(c)** *No magnetic island, $r/a = 1.0188$*

**(d)** *Magnetic islands, $r/a = 1.0188$*

**Figure 11:** *Normalized PDFs of density events along $(t, \varphi)$-axis at the LFS midplane and at two radial positions in the CFR and in the SOL, i.e. $r/a = 0.975$ (11a,11b) and $r/a = 1.0188$ (11c,11d). Cases with no magnetic island (11a,11c) in the simulation box. Cases with magnetic islands (11b,11d). As a reference, the dotted black line corresponds to an exact Gaussian. The color zones is the histogramm of each curve. The curves have been obtained with a kernel density estimation.*

## 5. Discussion

### 5.1. On the role of the $E \times B$ shear

An explanation of the changes observed on density profiles and turbulence properties could have been the decrease of the $E \times B$ shear $s_{E \times B}$ due to the flattening of the radial electric field's profile driven by the MPs. The radial profiles of $s_{E \times B}$ is shown on Fig. 13 for all the cases studied above. As could be expected from the potential profiles of Fig. 5 the MP reduces significantly the radial shear of the poloidal flow which one could be
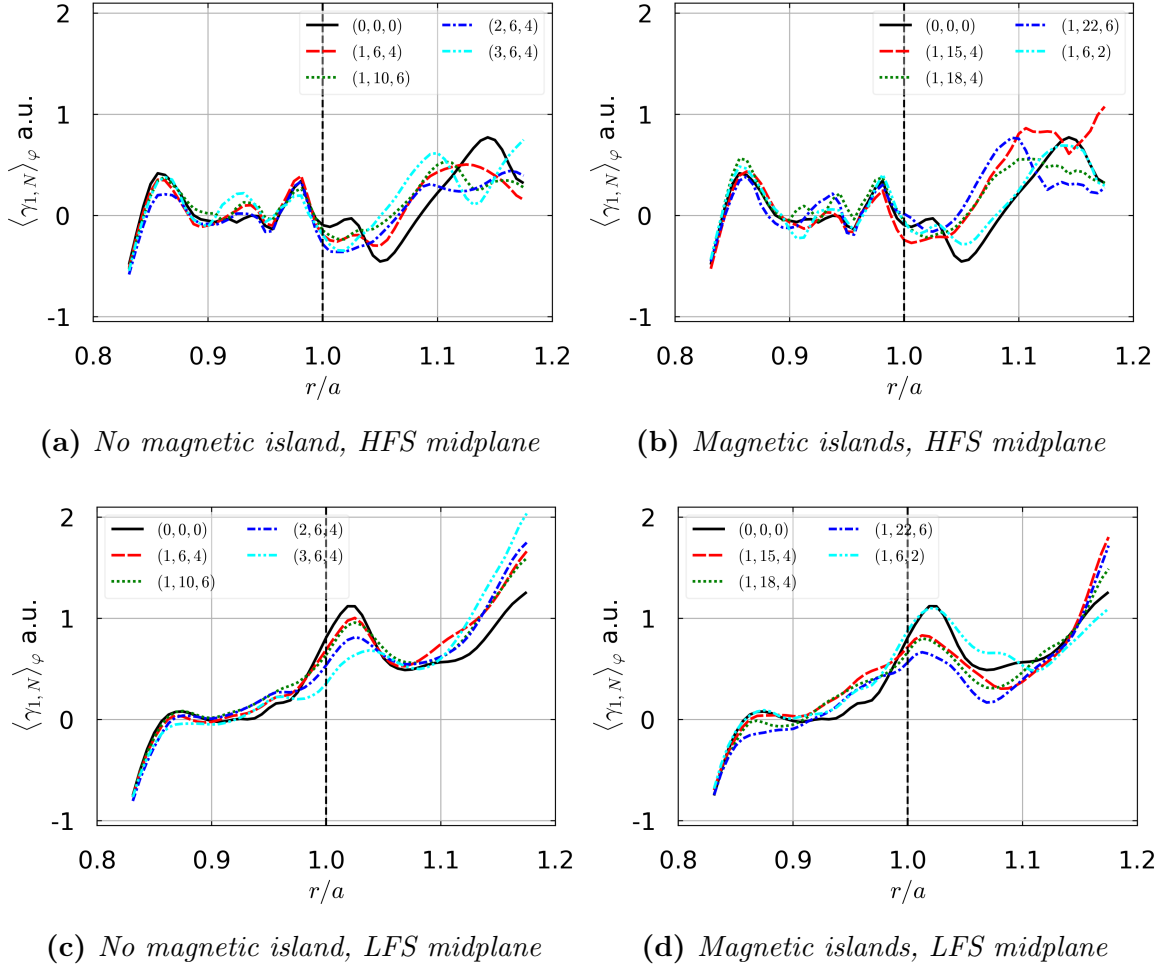
**(a)** *No magnetic island, HFS midplane*

**(b)** *Magnetic islands, HFS midplane*

**(c)** *No magnetic island, LFS midplane*

**(d)** *Magnetic islands, LFS midplane*

**Figure 12:** *Radial profiles of the skewness over time of the density, averaged over $\varphi$. HFS midplane (12a,12b). LFS midplane (12c,12d). The error bar for each curve is estimated to be smaller than 5%.*

tempted to associate with the increase of the turbulence flux and the flattening of the density profile. However, the reduction is much stronger for the non resonant modes than for the resonant ones, which is not the case for the other effects described above. This suggests that even if we can not exclude an influence of the change of the flow shear on turbulence transport, the shear reduction due to MPs is not the main mechanism explaining the changes in the turbulence pattern and in the mean density profiles.

## 5.2. Implications for mean field modelling

So far, the numerical analysis of the impact of RMPs on the edge equilibrium plasma including neutrals recycling have only been performed using mean-field codes [15]. In the absence of better indications, these studies are conducted assuming that perpendicular diffusion coefficients characterizing anomalous radial trasnport remain unchanged when RMPs are switched on. Our simulations allow us to cast some light on this assumption.
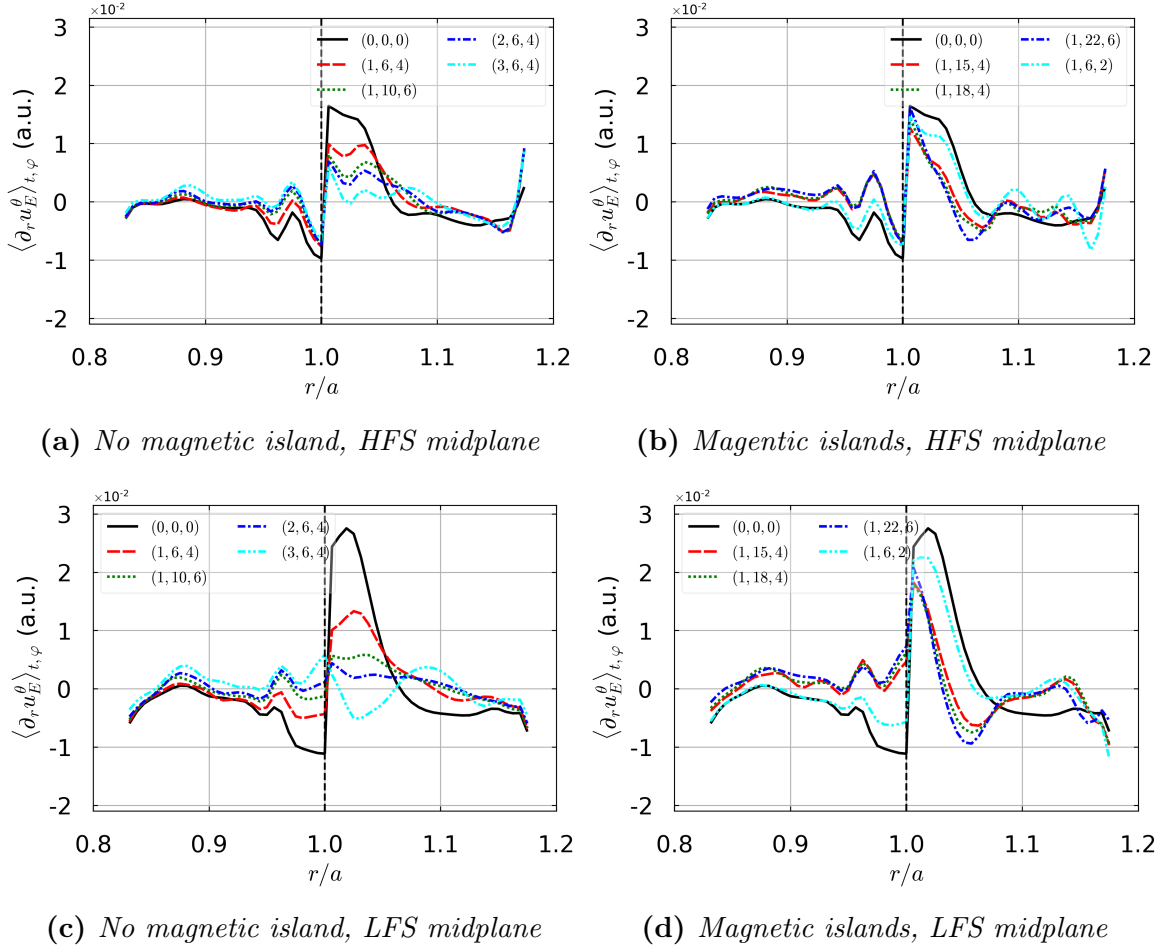
**(a)** *No magnetic island, HFS midplane*

**(b)** *Magentic islands, HFS midplane*

**(c)** *No magnetic island, LFS midplane*

**(d)** *Magnetic islands, LFS midplane*

**Figure 13:** *Radial profiles of the $E \times B$ shear averaged over $(t, \varphi)$ at the HFS midplane (13a,13b) and at the LFS midplane (13c,13d), $\langle s_{E \times B} \rangle_{t,\varphi} = \langle \partial_r u_{E \times B}^{\theta^*} \rangle_{t,\varphi}$. $\langle s_{E \times B} \rangle_{t,\varphi} = \langle \partial_r u_{E \times B}^{\theta^*} \rangle_{t,\varphi}$. MPs corresponding to magnetic islands into the computational domain (13b,13d) or not (13a),13c.*

To do so, in order to open a discussion on the relative impact of MPs on plasma equilibrium and plasma turbulence, 3D turbulence simulations have been compared to corresponding 3D transport simulations in which drifts have been switched off and anomalous transport is modelled by a constant diffusion coefficient. To perform such a comparison, an effective transport coefficient has been first computed from turbulence simulations. It has been defined as:

$$D_\perp = -\frac{\Gamma^r}{\nabla_r N} \tag{13}$$

Fig. 14 shows two examples of 2D maps in the poloidal plane of the time-averaged $D_\perp$ at $\varphi \sim \pi/2$. Results show a rather weak variations in the poloidal direction of this coefficient, with as expected highest values on the LFS (by removing the limiter area). A complete study we have performed, shows a global lowering of the averaged $D_\perp$ (in the same way as $\lambda_N$) when MPs are applied: $D_\perp = 3.3 \cdot 10^{-2}(\rho_L^2 \omega_c)$ for the reference solution $(0,0,0)$, and $D_\perp$ oscillates between $2.3 \cdot 10^{-2}$ and $2.8 \cdot 10^{-2}$ depending

on the perturbation, excepted for an unexplained reason for the MP $(1, 6, 2)$ for which $D_\perp = 3.8 \cdot 10^{-2}$.

For the present simulations, $D_\perp = 3.9 \cdot 10^{-2} \rho_L^2 \omega_c$ is considered. In addition, to avoid the occurence of small flow scales related to microturbulence the vorticity and the Ohm law equations are shunted. The perpendicular velocity $\vec{u}_\perp$ is put to zero and thus the radial transport is entirely modelled by $D_\perp$.
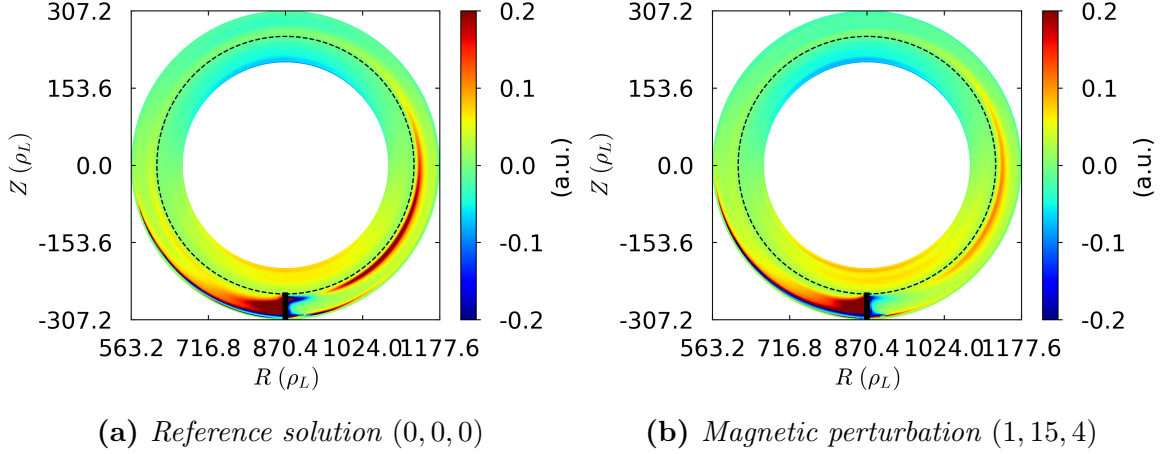


(a) *Reference solution* $(0, 0, 0)$     (b) *Magnetic perturbation* $(1, 15, 4)$

**Figure 14:** *2D map in the poloidal plane of the effective diffusion coefficient for the radial transport $D_\perp = \Gamma^\rho / \nabla_\rho N$, averaged in time and $\varphi$.*

We define the toroidal inhomogeneities of the time averaged density as:

$$(\langle N_{\mathrm{MP}} \rangle_t - \langle N_{(0,0,0)} \rangle_{t,\varphi}) / \langle N_{(0,0,0)} \rangle_{t,\varphi} \tag{14}$$

These inhomogeneities for 3D turbulence and corresponding transport computations are shown on Fig. 15 without MP, and with MPs $(1, 6, 2)$ and $(1, 15, 4)$ corresponding to two resonant modes, expected to provide a stronger impact. As expected the reference solution in transport mode (Fig. 15a) shows no inhomogeneity in the poloidal plane since the system is perfectly axisymmetric. In the reference turbulent case (see Fig. 15b), inhomogenities are visible at a level of around 6% due to the finite duration of our statistical interval and the strong correlation in the toroidal phasing between consecutive large scale events. Perturbated solutions clearly show now that the density fluctuations amplitude is enhanced in turbulence simulations compared to the corresponding transport ones, with respectively fluctuations amplitude of about $\pm 30\%$ for turbulence vs $\pm 3\%$ for transport. In addition, transport simulations clearly show that maximum fluctuations are localized on magnetic islands in the close vicinity of the separatrix (see Figs. 15c and 15e), which is not the case in turbulence simulations, Figs. 15d and 15f. In these latter simulations, the fluctuations maximum occurs into the SOL without any visible mode locking effect. The amplification by MPs of the toroidal inhomogeneities of the time-averaged density points out a possible phase locking of turbulence with respect to MPs, favouring specific poloidal/toroidal location for the radial propagation of the filaments in the SOL. The difference in the pattern of

homogeneities between the mean-field and the turbulent case also highlight a non local effect of the MP on turbulent transport.

## 6. Concluding remarks

This paper focused on the impact of 3D magnetic perturbations (MPs) on electrostatic and isothermal fluid turbulence at the edge of a limiter plasma in circular geometry. Single 3D mode MPs of small amplitude have been considered leading to magnetic islands or not in the computational domain depending on the wavenumbers combination in the poloidal and toroidal direction (resonant modes or not). This work is a first step towards a better understanding of the impact of magnetic perturbations. Results show an impact of MPs on the plasma equilibrium and on a lesser extent on the turbulence properties, with a magnitude which dependent on the MPs amplitude and on their wavenumbers, especially if they correspond to resonance with magnetic islands in the simulation box or not.

Concerning the plasma equilibrium, numerical results show an impact on profiles and flows and recover some key features seen in experiments such as the loss of density in the edge of the closed field lines region and the decrease of the radial electric field, coupled with a change of the plasma rotation. These changes of profiles are associated with a reorganisation of fluxes in the edge plasma, both mean field and turbulent, leading to strong changes and even local reversal of the parallel velocities (hence toroidal rotation). The latter effect had also been reported in experiments.

As far as exhaust issues are concerned, numerical results have shown that the MPs impact the SOL width, with a decrease of the SOL decay length. This is most probably related to the overall decrease of radial turbulent transport in the SOL, driven by a drop of the fluctuation level in the presence of a MPs.

Concerning the fluctuation properties, MPs do not change the fundamental nature of edge turbulence which remains dominated by intermittent large amplitude events associated with radially filamentary structures. Nevertheless, quantitative properties are impacted, especially in their spatial distribution (LFS/HFS asymmetries and radial profiles). MPs trigger a drop of the relative density fluctuation level in the near SOL. In the far SOL, the fluctuation level is found to decrease on the HFS but increase on the LFS. Intermittency, measured here as the skewness of the PDF of density fluctuations is also impacted, with a reduction in the vicinity of the separatrix in open field lines. On the opposite, an increase of the skewness of density fluctuation is observed in the outermost part of close field lines when magnetic islands are present. The latter effect is more marked when magnetic islands are present in the vicinity of the separatrix. We have noted a difference between LFS and HFS midplane, with a more important decrease of the skewness in the SOL, near the separtrix at LFS midplane compare to the HFS midplane. The skewness increase then at the HFS in the mid SOL whereas this
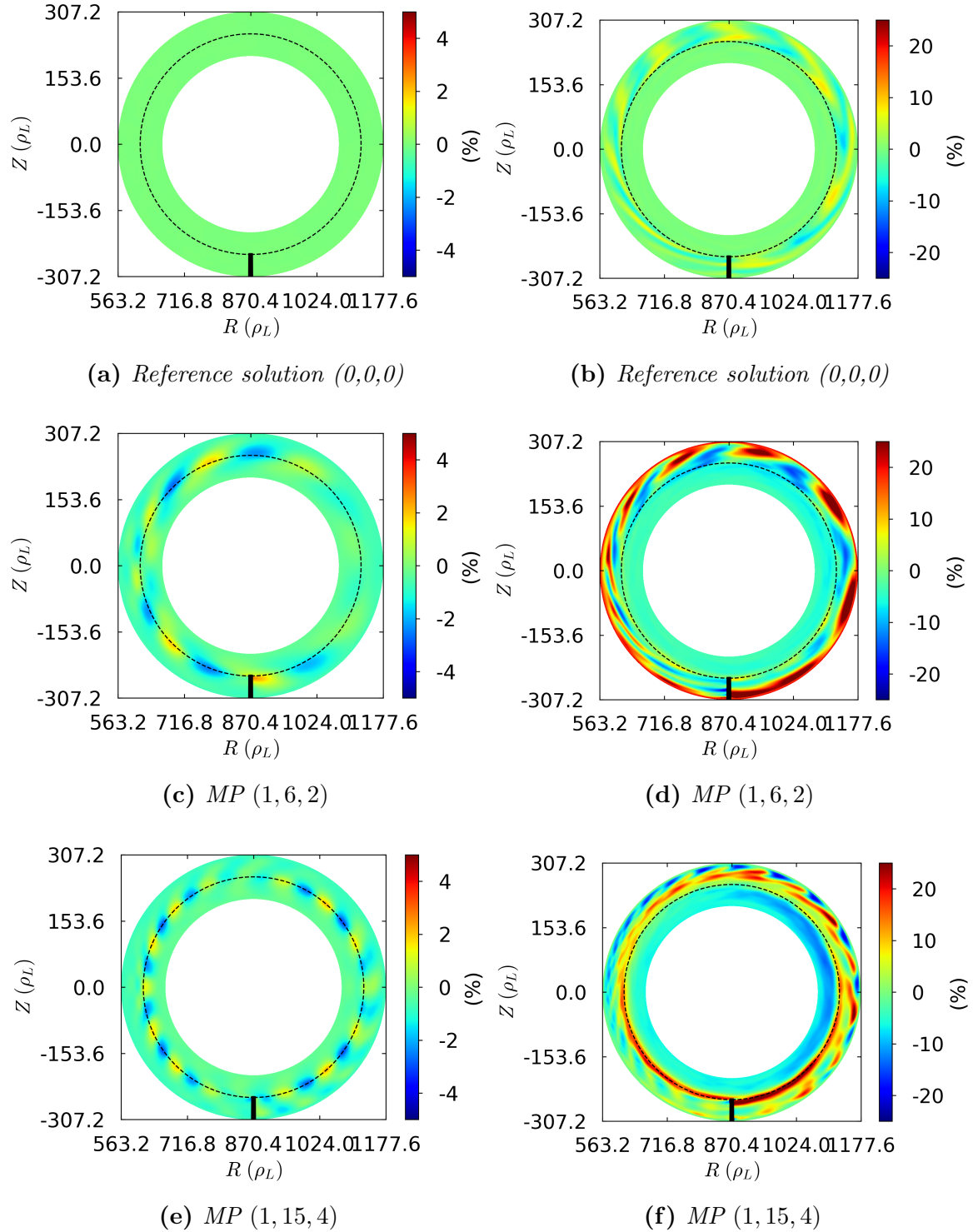
**(a)** *Reference solution (0,0,0)*

**(b)** *Reference solution (0,0,0)*

**(c)** *MP* $(1,6,2)$

**(d)** *MP* $(1,6,2)$

**(e)** *MP* $(1,15,4)$

**(f)** *MP* $(1,15,4)$

**Figure 15:** *2D maps in the poloidal plane $\varphi = 0$ of toroidal inhomogeneities of the time averaged density $(\langle N_{\mathrm{MP}}\rangle_t - \langle N_{(0,0,0)}\rangle_{t,\varphi})/\langle N_{(0,0,0)}\rangle_{t,\varphi}$. 3D transport simulations (15a,15c),15e. 3D turbulence simulations (15b,15d,15f). $D_\perp = 3.9 \cdot 10^{-2}\rho_L^2\omega_c$.*

increase is observed on the far SOL at the LFS only.

Finally, a comparison between self-consistent turbulence simulations and mean-field simulations, in which radial transport is prescribed via a gradient-diffusion assumption, highlight a significant difference in the response of the plasma to MPs. The amplitude of the non-axisymmetric density perturbation is much more pronounced in the self-consistent case than in the mean-field case. Moreover, its spatial localization is also different, the effect of magnetic islands remaining local in the mean-field case while non local effects are important with turbulence. These results suggest that the assumption of unperturbed perpendicular transport in mean-field simulations with MPs is probably an oversimplification and calls for further studies on the significant role played by turbulence on the response of the plasma to magnetic perturbations.

## 7. Aknowledgement

## Appendix A. Fluid equations

The TOKAM3X dimensionless equations for an isothermal plasma are given here. The magnetic field is assumed to be fixed and axisymmetric. The vector $\vec{b} = \vec{B}/B$ defines the direction of the magnetic field. The gradients in the parallel and perpendicular directions are respectively defined as $\nabla_\parallel \cdot = \vec{b} \cdot \nabla \cdot$ and $\nabla_\perp \cdot = \nabla \cdot - \vec{b} \nabla_\parallel \cdot$.

$$\partial_t N_i + \vec{\nabla} \cdot \left( \Gamma_i \vec{b} + N_i \vec{u}_{\perp,i} \right) = \vec{\nabla} \cdot (D_{\perp,N} \vec{\nabla}_\perp N_i) + S_N \tag{A.1}$$

$$\partial_t \Gamma_i + \vec{\nabla} \cdot \left( \frac{\Gamma_i^2}{N_i} \vec{b} + \Gamma_i \vec{u}_{\perp,i} \right) = -\vec{\nabla} \left( P_e + P_i \right)$$
$$+ \vec{\nabla} \cdot \left( D_{\perp,\Gamma} N_i \vec{\nabla}_\perp \frac{\Gamma_i}{N_i} + D_{\perp,N} \frac{\Gamma_i}{N_i} \vec{\nabla}_\perp N_i \right) + S_\Gamma \tag{A.2}$$

$$\partial_t W + \vec{\nabla} \cdot \left( W \frac{\Gamma_i}{N_i} \vec{b} + W(\vec{u}_E + \vec{u}_{\nabla B,i}) - J_\parallel \vec{b} \right) = \vec{\nabla} \cdot \left( N(\vec{u}_{\nabla B,i} - \vec{u}_{\nabla B,e}) \right)$$
$$+ \vec{\nabla} \cdot \left( D_{\perp,W} \vec{\nabla}_\perp W \right) + S_W \tag{A.3}$$

$$N_e \nabla_\parallel \Phi - \nabla_\parallel P_e - 0.71 N_e \nabla_\parallel T_e + \eta_\parallel N_i J_\parallel = 0 \tag{A.4}$$

where $N_{i,e}$ is the particle density for the ions or the electrons, $\Gamma_s = N_s u_{\parallel,i}$ is the parallel momentum, $J_\parallel$ the parallel current density and $P_{i,e} = N_{i,e} T_{i,e}$ is the pressure. Assuming quasineutrality $N_e = N_i = N$ and an isothermal plasma, it lets $P_i = P_e = N$ as $T_e = T_i = T = 1$.

Equ. A.3 is the electric charge balance. Eq. A.4 is the Ohm's law derived from the electron momentum balance equations by neglecting electron inertia. $D_\perp$ are diffusion coefficient, standing for sub-grid diffusion model representative of collisional transport processes. $\Phi$ is the electric potential and $\eta_\parallel$ the parallel resistivity. The generalized vorticity $W$, in the frame of the Boussinesq's approximation, is defined as:

$$W = \nabla \cdot \left( \frac{1}{B^2} \vec{\nabla}_\perp \Phi + \frac{1}{NB^2} \vec{\nabla}_\perp P_i \right) \tag{A.5}$$

Each equation gets a source term $S_X$ modelled in the code as a Gaussian with the peak at the core boundary. In this drift-reduced model, the perpendicular velocity is given by the following drift velocities:

$$\vec{u}_{\perp,i} = \vec{u}_E + \vec{u}_{\nabla B,i} + \vec{u}_{\text{curv}} = \frac{\vec{E} \times \vec{B}}{B^2} + \frac{2T_e}{B} \frac{\vec{B} \times \vec{\nabla}B}{B^2} + \frac{\Gamma_i^2}{N_i^2 B} \frac{\vec{B} \times \vec{\nabla}B}{B^2} \tag{A.6}$$

where $\vec{E} = -\vec{\nabla}\Phi$ is the electric field.

### *Appendix A.1. Boundary conditions*

In the perpendicular direction, a Neumann condition is used for all variables $\partial_\perp(\cdot) = 0$. In the SOL, at the sheath entrance, a Bohm-Chodura boundary conditions [30] are required on the Mach number: $M_\parallel \geq 1$ with $M_\parallel = u_{\parallel,i}/c_s = \Gamma_i/(N\sqrt{T_e + T_i})$. A parallel current $J_\parallel$ is imposed on each side of the target plate. These write (isothermal hypothesis):

$$(\Gamma_s \vec{b} + N_s \vec{u}_{\perp,s}) \cdot \vec{n} \geq N_s c_s \vec{b} \cdot \vec{n} \tag{A.7}$$

$$J_\parallel = \pm \Gamma_i (1 - e^{\Lambda - \Phi}) \underset{\Phi \to \Lambda}{\sim} N(\Lambda - \Phi) \tag{A.8}$$

where $\Lambda$ is the normalized sheath floating potential and $\vec{n}$ the normal to the wall. Using Eq. A.8 and the Ohm's law A.4, a condition on the parallel gradient of the electric potential is obtained:

$$\nabla_\parallel \Phi = \frac{\nabla_\parallel N}{N} \pm \eta_\parallel \Gamma_i (\Lambda - \Phi) \tag{A.9}$$

## Appendix B. Curvilinear coordinates system

In the following, the Einstein's convention is used (repeated indexes is a sum over possible values). With the covariant and contravariant basis (see Eq. 3 and 4) and the corresponding metric, the gradient, divergence and curl write:

$$\vec{\nabla} f = \frac{\partial f}{\partial u^i} \vec{e}^i \tag{B.1}$$

$$\vec{\nabla} \cdot f = \frac{1}{J} \frac{\partial}{\partial u^i} (Ja^i) \tag{B.2}$$

$$\vec{\nabla} \times f = \frac{1}{J} \sum_k \left( \frac{\partial a_j}{\partial u^i} - \frac{\partial a_i}{\partial u^j} \right) \vec{e}_k \quad i,j,k \text{ cyclic} \tag{B.3}$$

where $\vec{a}$ is a vector and $a^i = \vec{a} \cdot \vec{e}^i$, $a_i = \vec{a} \cdot \vec{e}_i$. $u^i \in \{\psi, \theta^*, \varphi\}$ (local basis). $J$ is the determinant of the local Jacobian matrix $\boldsymbol{J}$ defined in each point as:

$$\boldsymbol{J} = \begin{bmatrix} \partial R/\partial\psi & \partial R/\partial\theta^* & \partial R/\partial\varphi \\ \partial Z/\partial\psi & \partial Z/\partial\theta^* & \partial Z/\partial\varphi \\ \partial\phi/\partial\psi & \partial\phi/\partial\theta^* & \partial\phi/\partial\varphi \end{bmatrix} \approx \begin{bmatrix} \partial R/\partial\psi & \partial R/\partial\theta^* & 0 \\ \partial Z/\partial\psi & \partial Z/\partial\theta^* & 0 \\ 0 & 0 & \partial\phi/\partial\varphi \end{bmatrix} \tag{B.4}$$

We may notice that $\boldsymbol{J} = \vec{e}_i \cdot \vec{e}_j \times \vec{e}_k$ with $(i,j,k) \in (\psi, \theta^*, \varphi)$ in cyclic order. The parallel gradient then becomes:

$$\begin{aligned} \nabla_\parallel f &= \vec{b} \cdot \vec{\nabla} f \\ &= \frac{B_r}{B\sqrt{g_{\psi,\psi}}} \frac{\partial f}{\partial\psi} + \frac{B_p}{B\sqrt{g_{\theta^*,\theta^*}}} \frac{\partial f}{\partial\theta^*} + \frac{B_t}{B\sqrt{g_{\varphi,\varphi}}} \frac{\partial f}{\partial\varphi} \end{aligned} \tag{B.5}$$

and the divergence:

$$\vec{\nabla} \cdot (f\vec{b}) = \frac{1}{J} \left[ \frac{\partial}{\partial\psi} \left( Jf \frac{B_r}{B\sqrt{g_{\psi,\psi}}} \right) + \frac{\partial}{\partial\theta^*} \left( Jf \frac{B_p}{B\sqrt{g_{\theta^*,\theta^*}}} \right) + \frac{\partial}{\partial\varphi} \left( Jf \frac{B_t}{B\sqrt{g_{\varphi,\varphi}}} \right) \right] \tag{B.6}$$

The perpendicular gradient writes (contravariant basis):

$$\begin{aligned} \vec{\nabla}_\perp f &= \vec{\nabla} f - \vec{b} \nabla_\parallel f \\ &= \left[ \frac{\partial f}{\partial\psi} - \left( \frac{B_r \sqrt{g_{\psi,\psi}}}{B} + \frac{B_p \, g_{\theta^*,\psi}}{B\sqrt{g_{\theta^*,\theta^*}}} \right) \nabla_\parallel f \right] \vec{e}^\psi \\ &+ \left[ \frac{\partial f}{\partial\theta^*} - \left( \frac{B_r \, g_{\psi,\theta^*}}{B\sqrt{g_{\psi,\psi}}} + \frac{B_p \sqrt{g_{\theta^*,\theta^*}}}{B} \right) \nabla_\parallel f \right] \vec{e}^{\theta^*} \\ &+ \left[ \frac{\partial f}{\partial\psi} - \frac{B_t \sqrt{g_{\varphi,\varphi}}}{B} \nabla_\parallel f \right] \vec{e}^\varphi \end{aligned} \tag{B.7}$$

The drift velocities have the following expression (contravariant basis):

$$\begin{aligned} \frac{\vec{B} \times \vec{\nabla} f}{B^2} &= \frac{J}{B^2} \left[ \left( g^{\psi,\psi} \frac{B_t}{\sqrt{g_{\varphi,\varphi}}} \vec{e}^{\theta^*} - g^{\psi,\psi} \frac{B_p}{\sqrt{g_{\theta^*,\theta^*}}} \vec{e}^\varphi - g^{\psi,\theta^*} \frac{B_t}{\sqrt{g_{\varphi,\varphi}}} \vec{e}^\psi + g^{\psi,\theta^*} \frac{B_r}{\sqrt{g_{\psi,\psi}}} \vec{e}^\varphi \right) \frac{\partial f}{\partial\psi} \right. \\ &+ \left( g^{\theta^*,\psi} \frac{B_t}{\sqrt{g_{\varphi,\varphi}}} \vec{e}^{\theta^*} - g^{\theta^*,\psi} \frac{B_p}{\sqrt{g_{\theta^*,\theta^*}}} \vec{e}^\varphi - g^{\theta^*,\theta^*} \frac{B_t}{\sqrt{g_{\varphi,\varphi}}} \vec{e}^\psi + g^{\theta^*,\theta^*} \frac{B_r}{\sqrt{g_{\psi,\psi}}} \vec{e}^\varphi \right) \frac{\partial f}{\partial\theta^*} \\ &\left. + g^{\varphi,\varphi} \left( \frac{B_p}{\sqrt{g_{\theta^*,\theta^*}}} \vec{e}^\psi - \frac{B_r}{\sqrt{g_{\psi,\psi}}} \vec{e}^{\theta^*} \right) \frac{\partial f}{\partial\varphi} \right] \end{aligned} \tag{B.8}$$

## References

[1] F. Wagner. *Plasma Phys. Control. Fusion*, 49(12B):B1–B33, 2007.

[2] T. Eich et al. *Nucl. Fusion*, 53(9):093031, 2013.

[3] A. Scarabosio et al. *Journal Nucl. Materials*, 438:S426 – S430, 2013.

[4] R.A. Pitts et al. *Nucl. Materials and Energy*, 20:100696, 2019.

[5] A. W. Leonard. *Physics of Plasmas*, 21(9):090501, 2014.

[6] T. Eich et al. *Nucl. Materials and Energy*, 12:84 – 90, 2017.

[7] T.E. Evans. *Plasma Phys. Control. Fusion*, 57:123001, 2015.

[8] P. Tamain et al. *Plasma Phys. Control. Fusion*, 52:075017, 2010.

[9] A.J. Thornton et al. *Nucl. Fusion*, 54(6):064011, 2014.

[10] S. Mordijck et al. *Plasma Phys. Control. Fusion*, 58(1):014003, 2015.

[11] M. Becoulet et al. *Nucl. Fusion*, 52:054003, 2012.

[12] D. Reiser et al. *Phys. Plasmas*, 16(4):042317, 2009.

[13] F. Orain et al. *Plasma Phys. Control. Fusion*, 57(1):014020, 2014.

[14] Y. Feng et al. *Contributions to Plasma Physics*, 54(46):426–431, 2014.

[15] H. Frerichs et al. *Phys. Plasmas*, 23(6):062517, 2016.

[16] O. Schmitz et al. *Nucl. Fusion*, 56(6):066008, 2016.

[17] D. Reiser. *Phys. Plasmas*, 14:082314, 2007.

[18] J. Peer et al. *Nucl. Fusion*, 57(8):086026, 2017.

[19] P. Tamain et al. *Jour. Comp. Phys.*, 321:606–623, 2016.

[20] P. Beyer et al. *Plasma Phys. Control. Fusion*, 44(10):2167, 2002.

[21] D. Galassi et al. *Fluids*, 4(1):50, 2019.

[22] S.I. Braginskii. *Rev. Plasma Phys.*, 1:205, 1965.

[23] C. Baudoin et al. *Cont. Plasma Phys.*, 58(6-8):484–489, 2018.

[24] F. L. Hinton et al. *Rev. Mod. Phys.*, 48(2):239–308, 1976.

[25] T.E. Evans et al. *Nucl. Fusion*, 48(2):024002, 2008.

[26] Y. Liang et al. *Phys. Rev. Lett.*, 98:265004, 2007.

[27] J.W. Coenen et al. *Nucl. Fusion*, 51:063030, 2011.

[28] S.X. Wang et al. *Nucl. Fusion*, 58(11):112013, 2018.

[29] Y. Sarazin et al. *Phys. Plasmas*, 5(12):4214–4228, 1998.

[30] P.C. Stangeby. *The Plasma Boundary of Magnetic Fusion Devices*. CRC Press, 2000.